Numerical and Experimental Study of an Omnidirectional Vibro-Impact Nonlinear Energy Sink ISAE-SUPMECA

Auteur : Lami, Souhaïl
Promoteur(s) : Salles, Loïc
Faculté : Faculté des Sciences appliquées
Diplôme : Master en ingénieur civil en aérospatiale, à finalité spécialisée en "aerospace engineering"
Année académique : 2025-2026
URI/URL : http://hdl.handle.net/2268.2/26090

UNIVERSITE DE LIEGE
FACULTE DES SCIENCES APPLIQUEES

University of Liège – Faculty of Applied Sciences

EULER Laboratory, VAST-FM
ISAE-SUPMÉCA

Numerical and Experimental Study of an Omnidirectional Vibro-Impact Nonlinear Energy Sink

Scientific Report

Master's thesis submitted in partial fulfillment of the requirements for the degree of Master in Aerospace Engineering

Author: Souhaïl Lami

Academic supervisor: Loïc Salles

Internship supervisors: Stefania Lo Feudo, Stéphane Job

Academic Year: 2025 – 2026

June 9, 2026

Contents

List of Figures

Notation and conventions

Symbol	Description
N	NES
H	Host
G	Ground
$U_{i,x}$	Absolute position of body i along x, with $i \in \{N, H, G\}$
$U_{i,y}$	Absolute position of body i along y
$\dot{U}_{i,x}$	Absolute velocity of body i along x
$\dot{U}_{i,y}$	Absolute velocity of body i along y
$\ddot{U}_{i,x}$	Absolute acceleration of body i along x
$\ddot{U}_{i,y}$	Absolute acceleration of body i along y
θ_i	Angular position of body i, with $i \in \{N, H\}$
$\dot{\theta}_i$	Angular velocity of body i
$\ddot{\theta}_i$	Angular acceleration of body i
R_N	Radius of the NES
R_H	Radius of the Host
R_c	Contact radius, $R_c = R_H - R_N$
M_N	Mass of the NES
M_H	Mass of the Host
I_N	Moment of inertia of the NES
I_H	Moment of inertia of the Host
g	Gravitational acceleration
μ_c	Friction coefficient used in the impact law
μ_s	Friction coefficient between the NES and the supporting surface
ε	Normal restitution coefficient
β_0	Tangential restitution coefficient

Table 1: Notation and conventions used throughout the report.

Abstract

The objective of this work was to study an omnidirectional vibro-impact nonlinear energy sink composed of an internal cylindrical mass moving inside a circular Host. The work was divided into two main parts: the development of numerical models and the experimental study of several OVINES configurations.

First, a numerical OVINES model was developed in Python. The gravitational force was taken into account for the NES in order to perform different validation tests, including energy conservation and comparisons of rebound heights with theoretical values. Friction was then added to the model, and a new configuration with springs and dampers between the Host and the ground was also studied. This model shows that successive impacts transfer part of the energy from the Host to the NES and redistribute the motion among the translational and rotational degrees of freedom.

The second part of the work focused on the experimental study. A two-camera measurement setup was used to reconstruct the three-dimensional motion of the system. Several OVINES configurations were tested in order to reconstruct the relative trajectory of the NES, estimate its angular position and rotational velocity, detect impacts, and perform a first identification of the impact parameters.

A preliminary parameter identification was performed using selected impacts. The normal restitution coefficient was identified from five impacts, giving a mean value of approximately 0.72 and a standard deviation of 0.12. The collision friction coefficient and the tangential restitution coefficient were estimated from two selected impacts, giving indicative mean values of approximately $\overline{\mu}_{\mathrm{c}} = 0.129$ and $\overline{\beta_0} = 0.494$. These values should be considered as preliminary estimates due to the limited number of analysed impacts and the experimental limitations related to marker tracking, geometry reconstruction and measurement accuracy.

1 Introduction

Mechanical and civil engineering structures can be subjected to significant excitations, such as wind or earthquakes. These excitations can generate large vibrations capable of severely damaging the structure. A classical solution is the use of a Tuned Mass Damper (TMD). This device consists of adding a secondary mass, connected to the primary structure by a stiffness and a damper. Its natural frequency is tuned to a natural frequency of the primary system in order to reduce the vibratory response of the structure around this frequency. The main drawback of the TMD is that it is only effective over a narrow frequency band, and its performance decreases if the natural frequency of the structure or of the TMD changes [4].

One way to overcome this limitation is the use of Nonlinear Energy Sinks (NES). Unlike a linear absorber, a NES does not have a defined linear natural frequency. It can therefore act over a wider frequency range by inducing an energy transfer from the primary structure to the NES above a certain energy threshold.

There are several NES configurations, for example systems using nonlinear stiffnesses [5–7], magnetic effects [8–10], rotating masses [11], masses sliding along a curved track [12], or vibro-impact systems [4,13]. In this work, we focus more specifically on a Vibro-Impact Nonlinear Energy Sink (VI-NES) [14–17]. This type of device consists of a free mass placed inside a container. When the primary structure is excited, the mass can move and impact the walls of the container. Part of the vibratory energy is then dissipated during the collisions [14–17].

In this study, an OVINES system is investigated, using an instantaneous impact model to describe the collisions between the NES and the wall of the container. The motion of the NES is described along the horizontal x and y directions, as well as in rotation. Friction is also taken into account in the model [1, 2, 18]. An experimental study is then carried out in order to observe the dynamics of the real system and to initiate a calibration of the numerical model. This experimental part makes it possible to extract the trajectory of the NES, estimate its rotation, and begin the identification of some model parameters, especially those related to collisions and friction.

Part I

Numerical Models

This section introduces the general numerical model used to describe the motion of the NES inside the circular Host. The equations of motion are first established between two successive impacts, before introducing the contact law used when the NES reaches the Host wall.

2 General OVINES model

The objective of this part is to develop and validate a numerical model of an omnidirectional vibro-impact nonlinear energy sink (OVINES). An OVINES is a passive vibration absorber in which an internal mass moves freely inside a container and dissipates energy through successive impacts with the container wall.

The system considered in this first model consists of an internal cylindrical mass, called NES and denoted by N, moving inside a circular Host container, denoted by H. The geometry and the main variables of the model are shown in Fig. 1. The aim of this preliminary model is not yet to reproduce the complete experimental setup, but rather to validate the numerical implementation of the free-flight dynamics, the impact detection procedure and the collision law.

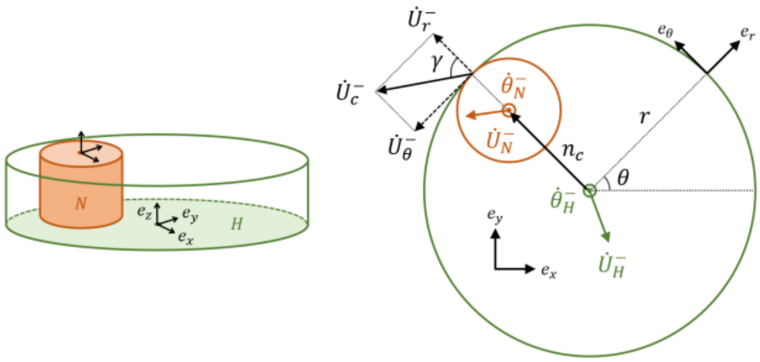

Figure 1: Diagram of the studied OVINES system and definition of the local contact frame.

The collision model used to update the velocities at impact is based on the formulation proposed by Luding [18]. Between two impacts, the equations of motion are integrated using the `solve_ivp` function from the `SciPy` library. The contact condition is defined as an event function, allowing the integration to stop precisely when an impact occurs. The collision law is then applied, and the integration is restarted with the updated velocities.

2.1 Dynamics of the system

Between two successive impacts, the motion of the internal mass and of the Host is governed by classical Newtonian dynamics. In the general case, the equations of motion can be written in second-order form as

$$M_N \ddot{\mathbf{U}}_N = \mathbf{F}_N, \tag{1}$$

$$M_H \ddot{\mathbf{U}}_H = \mathbf{F}_H, \tag{2}$$

where $\mathbf{U}_N$ and $\mathbf{U}_H$ are respectively the position vectors of the NES and of the Host, and where $\mathbf{F}_N$ and $\mathbf{F}_H$ denote the external forces applied to each body.

In the first model considered here, the internal mass is subjected only to gravity, while the Host is assumed to be fixed and is not subjected to any external excitation. Therefore, the equations of motion reduce to

$$\ddot{U}_{N,x} = 0, \qquad \ddot{U}_{N,y} = -g, \tag{3}$$

$$\ddot{U}_{H,x} = 0, \qquad \ddot{U}_{H,y} = 0. \tag{4}$$

The rotational degrees of freedom are also included in the state vector. Since no external torque is applied between two impacts, the angular accelerations are equal to zero:

$$\ddot{\theta}_N = 0, \qquad \ddot{\theta}_H = 0. \tag{5}$$

In order to solve the system numerically using the `solve_ivp` function from the `SciPy` library, the second-order equations are rewritten as a first-order system. For this purpose, the state vector is defined as

$$\mathbf{y} = \begin{pmatrix} U_{N,x} \\ U_{N,y} \\ \dot{U}_{N,x} \\ \dot{U}_{N,y} \\ \theta_N \\ \dot{\theta}_N \\ U_{H,x} \\ U_{H,y} \\ \dot{U}_{H,x} \\ \dot{U}_{H,y} \\ \theta_H \\ \dot{\theta}_H \end{pmatrix}. \tag{6}$$

The time derivative of the state vector can then be written as

$$\frac{d\mathbf{y}}{dt} = f(t, \mathbf{y}) = \begin{pmatrix} \dot{U}_{N,x} \\ \dot{U}_{N,y} \\ 0 \\ -g \\ \dot{\theta}_N \\ 0 \\ \dot{U}_{H,x} \\ \dot{U}_{H,y} \\ 0 \\ 0 \\ \dot{\theta}_H \\ 0 \end{pmatrix}. \tag{7}$$

The system can therefore be integrated numerically between two impacts. The contact condition is monitored during the integration using an event function. An impact is detected when the distance between the centers of the NES and the Host reaches the contact radius:

$$\|\mathbf{r}_N - \mathbf{r}_H\| - R_c = 0, \qquad R_c = R_H - R_N. \tag{8}$$

When this condition is satisfied, the time integration is stopped, the impact law is applied to update the translational and angular velocities, and the integration is restarted with the updated state vector.

2.2 Numerical implementation

2.2.1 Choice of characteristic units

In order to improve the numerical conditioning of the problem, the equations are written in dimensionless form. Since the internal mass is subjected to gravity, the characteristic quantities are defined from the contact radius $R_c = R_H - R_N$ and the gravitational acceleration g. The characteristic length, time, velocity and angular velocity are chosen as

$$L_0 = R_c, \tag{9}$$

$$T_0 = \sqrt{\frac{L_0}{g}}, \tag{10}$$

$$V_0 = \frac{L_0}{T_0} = \sqrt{gL_0}, \tag{11}$$

$$\omega_0 = \frac{1}{T_0}. \tag{12}$$

The positions are therefore non-dimensionalized by L_0, the translational velocities by V_0, and the angular velocities by ω_0. The angular positions are already dimensionless and are therefore not modified.

2.2.2 Non-dimensional formulation

Before the numerical integration, the initial conditions and the model parameters are converted into dimensionless quantities. The state vector is written as

$$\mathbf{y} = \begin{pmatrix} U_{N,x} \\ U_{N,y} \\ \dot{U}_{N,x} \\ \dot{U}_{N,y} \\ \theta_N \\ \dot{\theta}_N \\ U_{H,x} \\ U_{H,y} \\ \dot{U}_{H,x} \\ \dot{U}_{H,y} \\ \theta_H \\ \dot{\theta}_H \end{pmatrix}. \tag{13}$$

In dimensionless form, the gravitational acceleration becomes equal to one. The equations of motion between two impacts can then be integrated in a normalized form, which improves the numerical stability and avoids working with quantities of very different orders of magnitude.

2.2.3 Numerical integration and event detection

The equations of motion are integrated using the `solve_ivp` function from the `SciPy` library. The integration is performed between two successive impacts. The contact condition is introduced as an event function:

$$\|\mathbf{r}_N - \mathbf{r}_H\| - R_c = 0, \tag{14}$$

where $R_c = R_H - R_N$ is the contact radius.

The `terminal` option of the event makes it possible to stop the integration of `solve_ivp` at the time of the event. The `direction` option, when positive, implies that the event is detected only if the internal mass exits the container and not in the opposite direction. The direction is therefore chosen to be positive in order to avoid cases of "external rebound" that could be detected.

Indeed, `solve_ivp` computes the positions and velocities of the two objects at each time step. When the event condition is encountered, it stops the integration and applies a root-finding algorithm, based on Brent's method, to accurately determine the time of contact. However, it was observed that this algorithm finds this root with a precision of the order of 10^{-16}, such that, at the time of contact, it sometimes returns a distance between the internal mass and the container equal to

$$\|\mathbf{r}_N - \mathbf{r}_H\| = R_c + \alpha \times 10^{-16}, \qquad \alpha \in [1, \dots, 9]. \tag{15}$$

Thus, at the next iteration, a parasitic event could be triggered and lead to an external rebound. This is avoided by choosing `direction = +1`.

The event option of `solve_ivp` therefore makes it possible to stop the integration at the time of contact between the internal mass and the wall, in order to apply the contact model, which returns the new velocities after contact. These velocities are then returned to `solve_ivp`, which resumes the integration until the next contact.

2.2.4 Stopping criterion

A stopping criterion on the maximum number of rebounds was implemented in order to prevent the code from running indefinitely in some cases.

2.3 Validation tests

2.3.1 Simple operating tests

In this first series of tests, a container with a very large mass is considered, so that the container practically does not move. $R_N = 1$, $R_H = 10$, $M_N = 1$, $M_H = 10^9$.

Test 1

In this test, the internal mass is released at the center of the container without initial velocities and with a restitution coefficient $\varepsilon = 1$. The mass is expected to fall and then rise back to its initial height indefinitely.

Table 2: Impact and initial condition parameters

Parameter	**Value**
Friction coefficient μ_c	0
Restitution coefficient ε	1
Tangential restitution β_0	0
Initial state $\mathbf{y}_0$	$(U_{N,x}, U_{N,y}, \dot{U}_{N,x}, \dot{U}_{N,y}, \theta_N, \dot{\theta}_N, U_{H,x}, U_{H,y}, \dot{U}_{H,x}, \dot{U}_{H,y}, \theta_H, \dot{\theta}_H)$
Values	$(0, 0, 0, 0, 0, 0,\ 0, 0, 0, 0, 0, 0)$

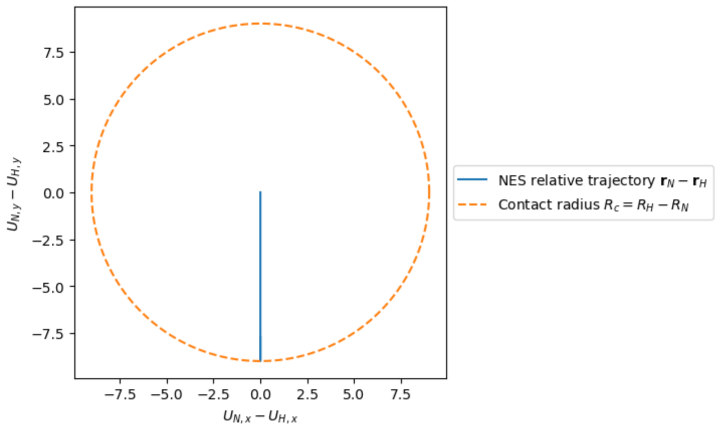

(a) Relative trajectory of the NES

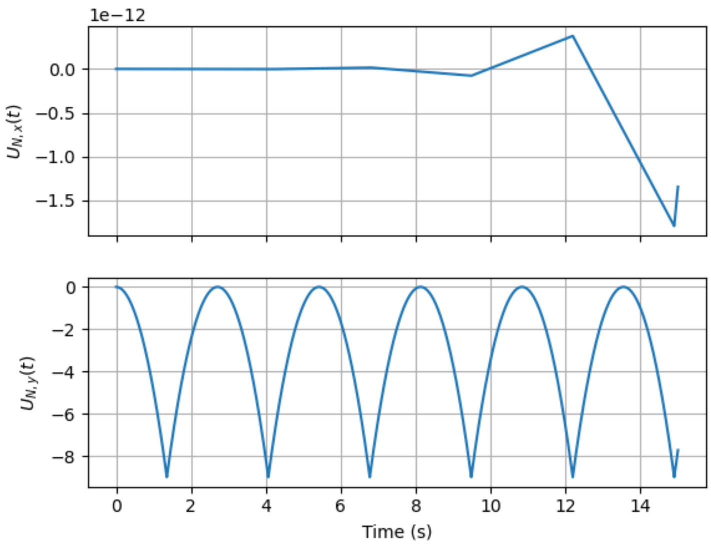

(b) Time evolution of the NES

Figure 2: Simulation of the vertical rebound test with $\varepsilon = 1$.

The expected result is indeed observed.

Test 2

Test similar to the previous test with a restitution coefficient $\varepsilon = 0.9$. The height after rebound is expected to decrease progressively. The height after each rebound can be determined analytically using the following derivation:

$$M_N g H_0 = \frac{1}{2} M_N v_{N,0}^2 \text{ Conservation of energy} \tag{16}$$
$$v_{N,0} = \sqrt{2gH_0} \tag{17}$$
$$v_{N,1} = \varepsilon v_{N,0} \tag{18}$$
$$M_N g H_1 = \frac{1}{2} M_N v_{N,1}^2 \text{ Conservation of energy} \tag{19}$$
$$H_1 = \varepsilon^2 H_0 \tag{20}$$
$$\Rightarrow H_n = \varepsilon^{2n} H_0 \tag{21}$$

Thus, the maximum height decreases by a factor ε^2 after each rebound. The numerically obtained values can then be compared with the theoretical values.

For this test, the container is fixed, in order to evaluate more precisely the errors on the rebound heights.

Table 3: Impact and initial condition parameters

Parameter	**Value**
Friction coefficient μ_c	0
Restitution coefficient ε	0.9
Tangential restitution β_0	0
Initial state $\mathbf{y}_0$	$(U_{N,x}, U_{N,y}, \dot{U}_{N,x}, \dot{U}_{N,y}, \theta_N, \dot{\theta}_N, U_{H,x}, U_{H,y}, \dot{U}_{H,x}, \dot{U}_{H,y}, \theta_H, \dot{\theta}_H)$
Values	$(0, 0, 0, 0, 0, 0,\ 0, 0, 0, 0, 0, 0)$

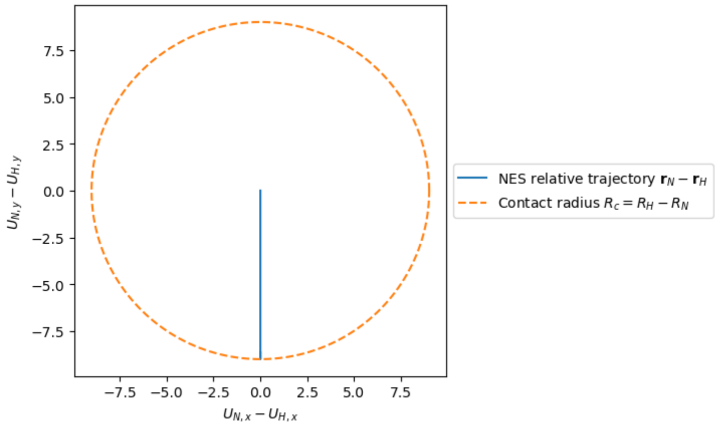

(a) Relative trajectory of the NES

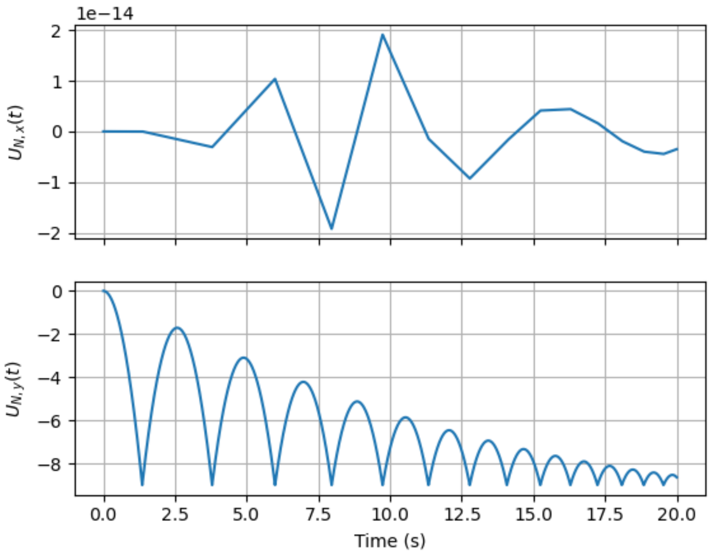

(b) Time evolution of the NES

Figure 3: Simulation results for the vertical rebound test with $\varepsilon = 0.9$.

The errors between the numerical values of the rebound heights and the theoretical values are displayed in the following Figures.

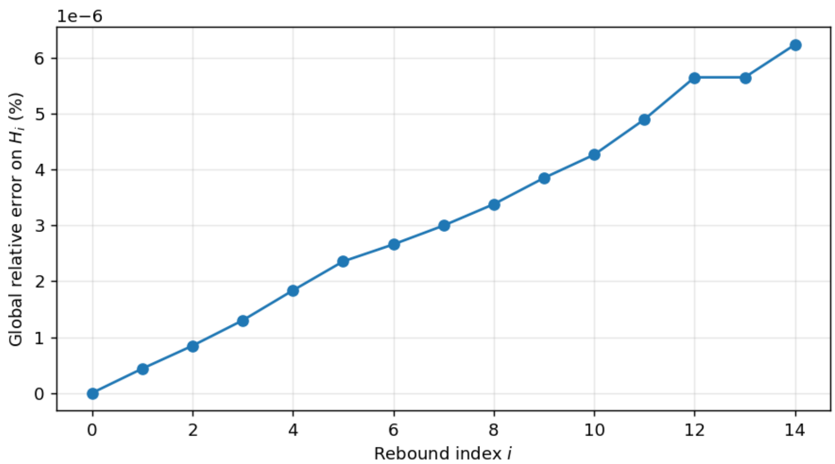

Figure 4: Global relative error between the numerical and theoretical rebound heights.

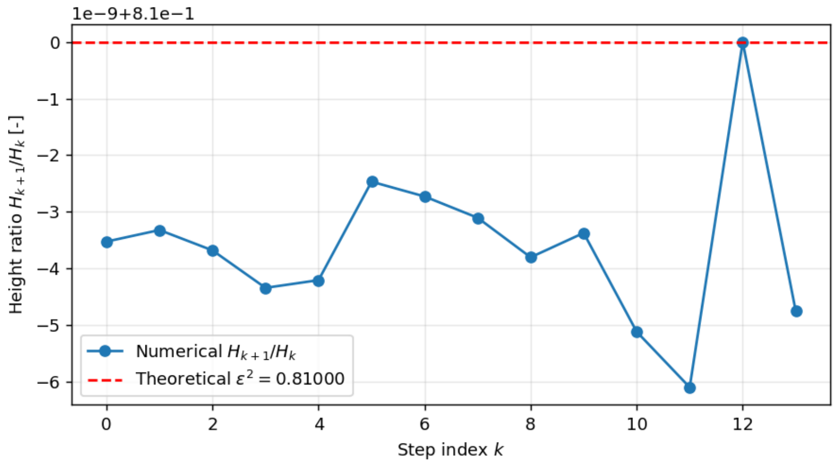

Figure 5: Comparison between the numerical and theoretical ratios of successive rebound heights.

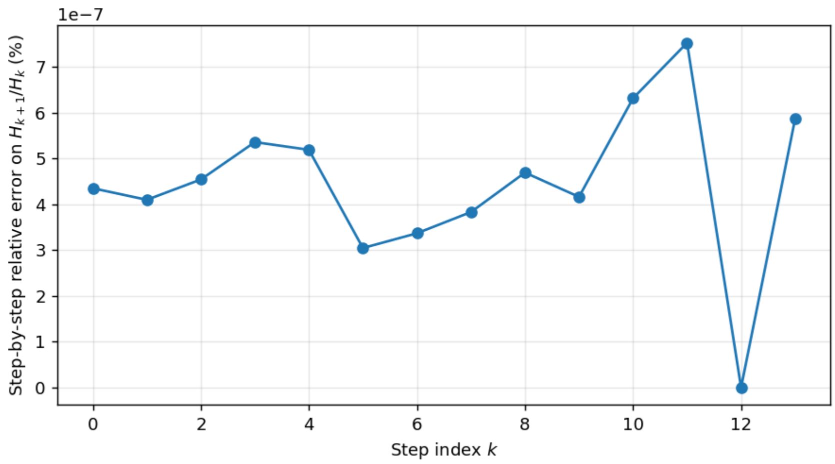

Figure 6: Relative error on the rebound height ratio between two successive rebounds.

It is observed in Figure 6 that the errors between each rebound are of the order of 10^{-7}.

3 Friction

This section introduces the friction model added to the numerical formulation.

3.1 Coulomb smooth model

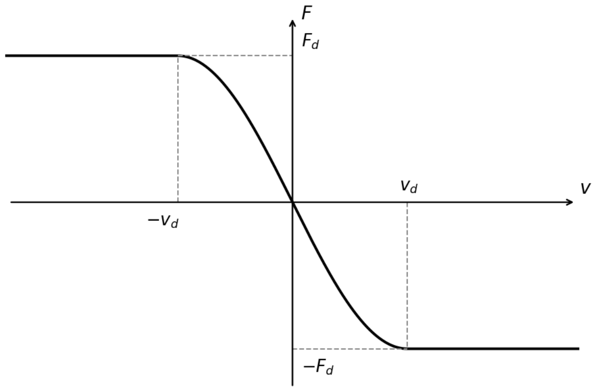

Figure 7: *Coulomb smooth* regularization using a hyperbolic tangent function.

First, a simple friction model was implemented: the *Coulomb smooth* model (continuous model). It makes it possible to avoid the discontinuity in the vicinity of $v = 0$. Several representations exist; in this project, the hyperbolic tangent regularization is used:

$$F_{\text{friction}} = -\mu_{\text{s}} F_{\text{N}} \tanh\left(\frac{v}{v_d}\right), \tag{22}$$

where μ_{s} is the dynamic friction coefficient, F_{N} the normal force and v_d a velocity regularization parameter. A compromise between accuracy and numerical cost will be sought for the choice of v_d.

Simple test (energy balance)

A cylinder (or disk) sliding on a horizontal ground with an initial velocity v_0 is considered. The equation of motion is:

$$m\,\ddot{u} = -\mu_{\text{s}} m g \tanh\left(\frac{v}{v_d}\right). \tag{23}$$

With friction, the theoretical stopping distance obtained by conservation of energy is written as:

$$E_{\text{kin},0} = \frac{1}{2} m v_0^2, \tag{24}$$

$$W = -\mu_{\text{s}} m g\, d, \tag{25}$$

$$\Rightarrow \quad d = \frac{v_0^2}{2\mu_{\text{s}} g}. \tag{26}$$

With $v_0 = \sqrt{10}\,\text{m/s}$, $\mu_{\text{s}} = 0.5$ and $g = 10\,\text{m/s}^2$, one obtains $d = 1\,\text{m}$.

Non-dimensionalization. The following quantities are introduced:

$$V_0 = v_0, \tag{27}$$

$$T_0 = \frac{V_0}{\mu_s g} \qquad \text{(this choice simplifies the translational equation).} \tag{28}$$

The dimensionless variables are:

$$\tau = \frac{t}{T_0}, \qquad \tilde{u} = \frac{u}{L_0}, \qquad L_0 = V_0 T_0. \tag{29}$$

With $v = V_0 \tilde{v}$ and $t = T_0 \tau$, one has:

$$\ddot{u} = \frac{L_0^2}{T_0^2} \frac{d^2 \tilde{u}}{d\tau^2}. \tag{30}$$

By substituting and using $\frac{V_0}{T_0} = \mu_s g$, one obtains:

$$\frac{d^2 \tilde{u}}{d\tau^2} = -\tanh\left(\frac{\tilde{v}}{\tilde{v}_d}\right), \qquad \tilde{v}_d = \frac{v_d}{V_0}. \tag{31}$$

By numerically solving the system using `solve_ivp`, the following curves are obtained:

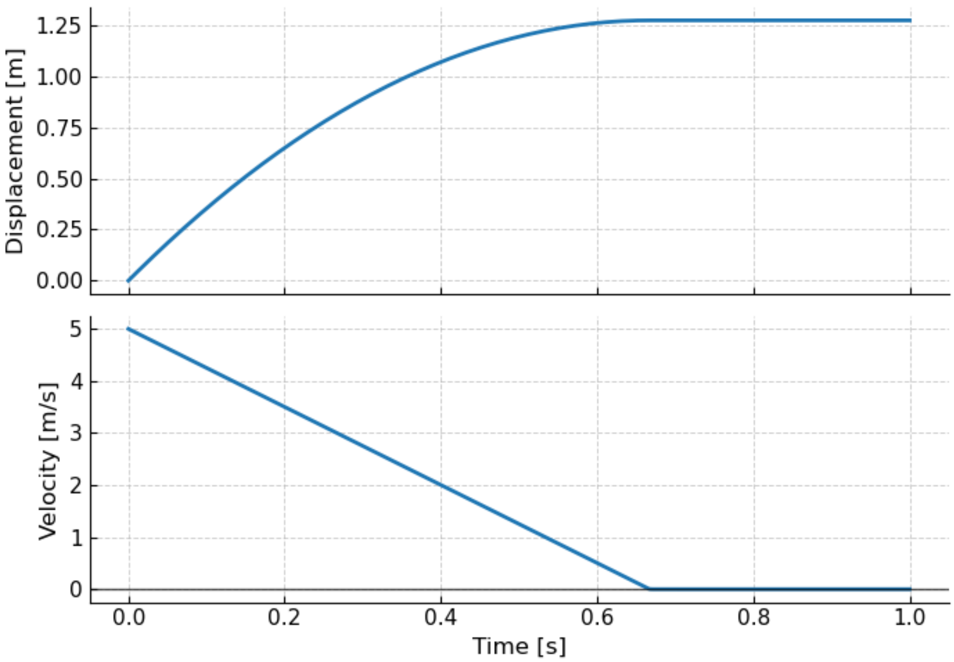

Figure 8: Simple test: evolution of the position and velocity in the presence of a *Coulomb smooth* friction.

It is observed that the cylinder indeed stops after a distance of 1 m: this simple test is therefore verified.

3.2 Rabinowicz test

The implementation of the *Coulomb smooth* model is then verified through the Rabinowicz test, by comparing the results to those of [1]. The test consists of a mass m connected to a spring of stiffness k, subjected to friction on a ground moving at the velocity v_{ground} (Fig. 9).

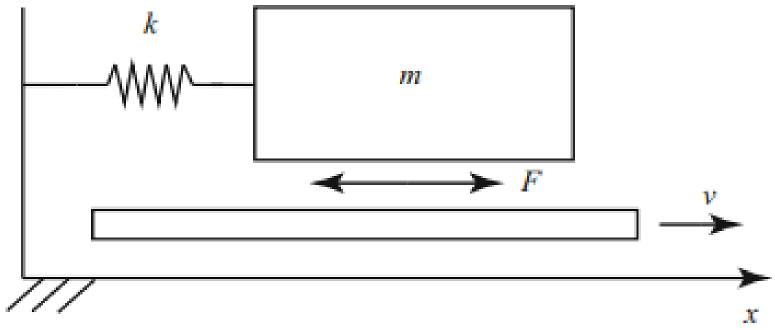

Figure 9: Rabinowicz test (figure reproduced from [1]).

By denoting u the displacement of the mass, and $v_{\text{rel}} = \dot{u} - v_{\text{ground}}$ the relative velocity, the equation of motion is:

$$m\ddot{u} = -\mu_d mg \tanh\left(\frac{\dot{u} - v_{\text{ground}}}{v_d}\right) - ku. \tag{32}$$

The parameters from [1] are:

$$m = 20 \text{ kg}, \qquad g = 9.81 \text{ m} \cdot \text{s}^{-2}, \qquad k = 10 \text{ N} \cdot \text{m}^{-1}, \tag{33}$$

$$\mu_d = 0.5, \qquad v_d = 0.05 \text{ m} \cdot \text{s}^{-1}, \qquad v_{\text{ground}} = 0.5 \text{ m} \cdot \text{s}^{-1}. \tag{34}$$

Initial conditions:

$$u(0) = 0, \qquad \dot{u}(0) = 0.5 \text{ m} \cdot \text{s}^{-1}. \tag{35}$$

Non-dimensionalization

One chooses:

$$V_0 = v_0, \tag{36}$$

$$\omega_0 = \sqrt{\frac{k}{m}}, \tag{37}$$

$$T_0 = \frac{1}{\omega_0}, \tag{38}$$

$$L_0 = V_0 T_0. \tag{39}$$

Dimensionless variables:

$$\tau = \frac{t}{T_0}, \qquad \tilde{u} = \frac{u}{L_0}, \qquad \tilde{v} = \frac{\dot{u}}{V_0}, \qquad \tilde{v}_{\text{ground}} = \frac{v_{\text{ground}}}{V_0}, \qquad \tilde{v}_d = \frac{v_d}{V_0}. \tag{40}$$

Then

$$\ddot{u} = \frac{L_0^2}{T_0^2} \frac{d^2\tilde{u}}{d\tau^2}. \tag{41}$$

By substituting into the equation of motion and using $L_0 = V_0 T_0$ and $T_0^2 = m/k$, one obtains:

$$\frac{d^2\tilde{u}}{d\tau^2} = -\alpha \tanh\left(\frac{\tilde{v} - \tilde{v}_{\text{ground}}}{\tilde{v}_d}\right) - \tilde{u}, \tag{42}$$

with

$$\alpha = \frac{\mu_d g}{\omega_0 V_0}. \tag{43}$$

The dimensionless initial conditions are:

$$\tilde{u}(0) = 0, \qquad \frac{d\tilde{u}}{d\tau}(0) = 1. \tag{44}$$

Results

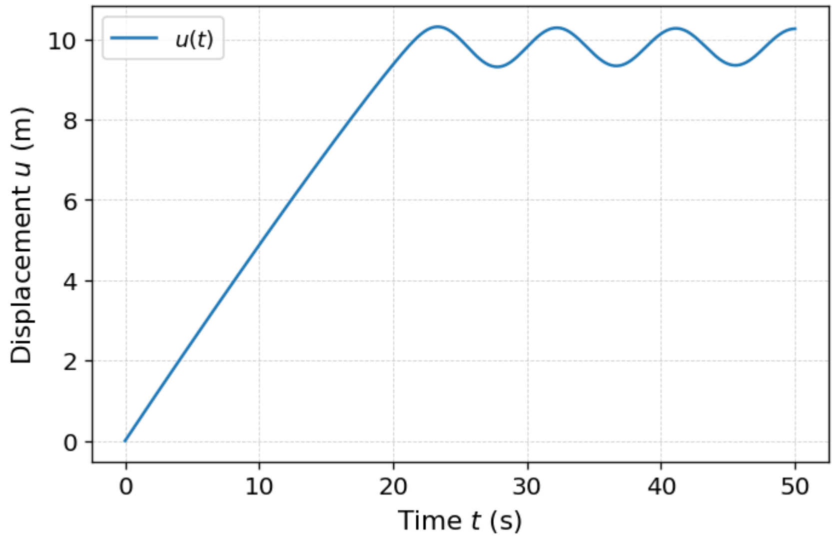

Figure 10: Rabinowicz test: evolution of the displacement $u(t)$ (*Coulomb smooth* model).

The result of Fig. 10 is in agreement with that of [1].

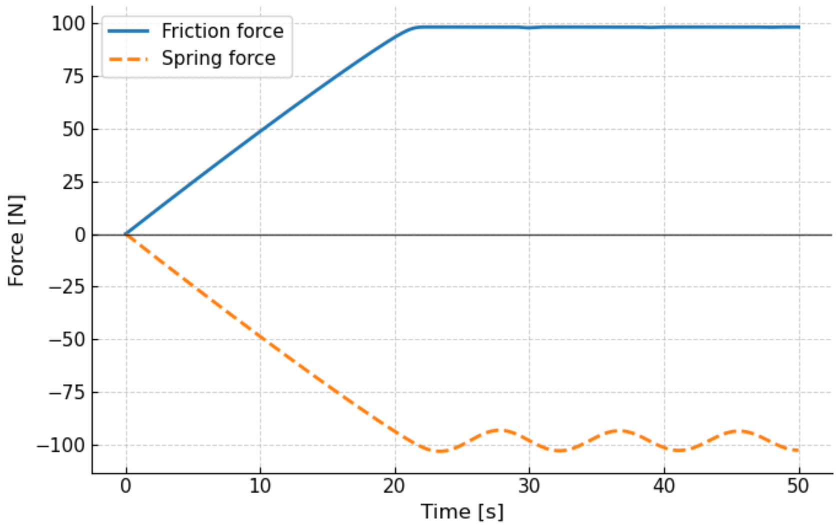

Figure 11: Rabinowicz test: friction forces and stiffness force as a function of time.

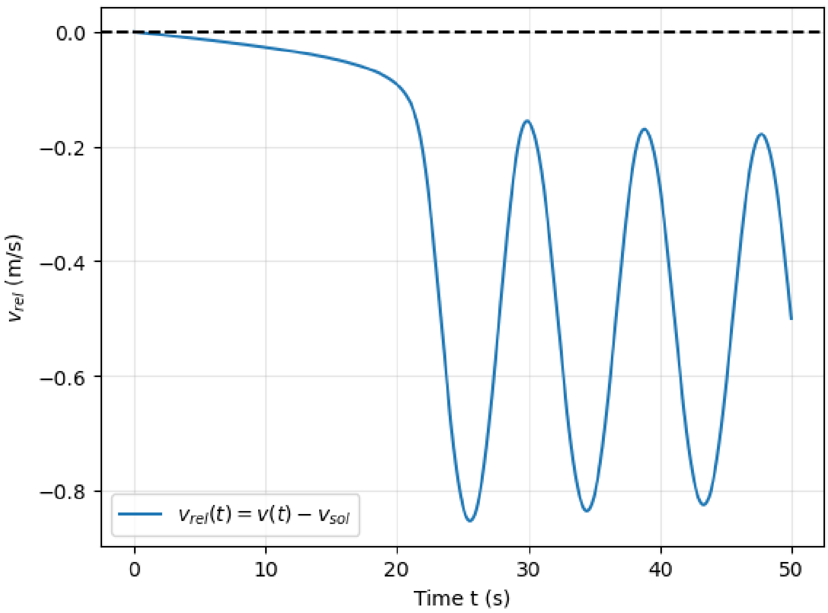

Figure 12: Rabinowicz test: relative velocity $v_{\mathrm{rel}}(t) = \dot{u}(t) - v_{\mathrm{ground}}$.

As shown in Fig. 11, the friction force opposes the stiffness force until it reaches its threshold $\mu_d mg$, after which the system enters an oscillatory regime. Fig. 12 highlights that v_{rel} remains small but non-zero: the *Coulomb smooth* model therefore does not reproduce stiction exactly.

3.3 Friction model in translation and rotation

3.3.1 Farkas model

Remark: In this section only, the parameter ε denotes the velocity ratio of the Farkas friction model and must not be confused with the normal restitution coefficient used elsewhere in the report.

In the context of this project, the internal mass is also rotating. It is therefore necessary to represent friction in rotation. For this, the model proposed in [2] is considered, in which the friction forces in translation and rotation are written as:

$$F_{\mathrm{friction,trans}} = -\mu_{\mathrm{s}} mg\,\mathcal{F}(\varepsilon), \tag{45}$$

$$M_{\mathrm{friction,rot}} = -\mu_{\mathrm{s}} mgR\,\mathcal{T}(\varepsilon), \tag{46}$$

with

$$\varepsilon = \frac{|v|}{R|\omega|}. \tag{47}$$

The functions $\mathcal{F}(\varepsilon)$ and $\mathcal{T}(\varepsilon)$ are given by:

$$\mathcal{F}(\varepsilon) = \begin{cases} \dfrac{4}{3}\,\dfrac{(\varepsilon^2+1)E(\varepsilon) + (\varepsilon^2-1)K(\varepsilon)}{\varepsilon\pi}, & \varepsilon \le 1, \\[2ex] \dfrac{4}{3}\,\dfrac{(\varepsilon^2+1)E\left(\dfrac{1}{\varepsilon}\right) - (\varepsilon^2-1)K\left(\dfrac{1}{\varepsilon}\right)}{\pi}, & \varepsilon \ge 1, \end{cases} \tag{48}$$

$$\mathcal{T}(\varepsilon) = \begin{cases} \dfrac{4}{9} \dfrac{(4-2\varepsilon^2)E(\varepsilon) + (\varepsilon^2-1)K(\varepsilon)}{\pi}, & \varepsilon \leq 1, \\ \dfrac{4\varepsilon}{9} \dfrac{(4-2\varepsilon^2)E\left(\dfrac{1}{\varepsilon}\right) + (2\varepsilon^2 - 5 + \dfrac{3}{\varepsilon^2})K\left(\dfrac{1}{\varepsilon}\right)}{\pi}, & \varepsilon \geq 1. \end{cases} \tag{49}$$

where $K(\varepsilon)$ and $E(\varepsilon)$ are the complete elliptic integrals of the first and second kind [19]. The associated equations of motion are:

$$m\frac{dv}{dt} = -\mu_s mg\,\mathcal{F}(\varepsilon), \tag{50}$$

$$I\frac{d\omega}{dt} = -\mu_s mgR\,\mathcal{T}(\varepsilon). \tag{51}$$

The following results are reported in [2]:

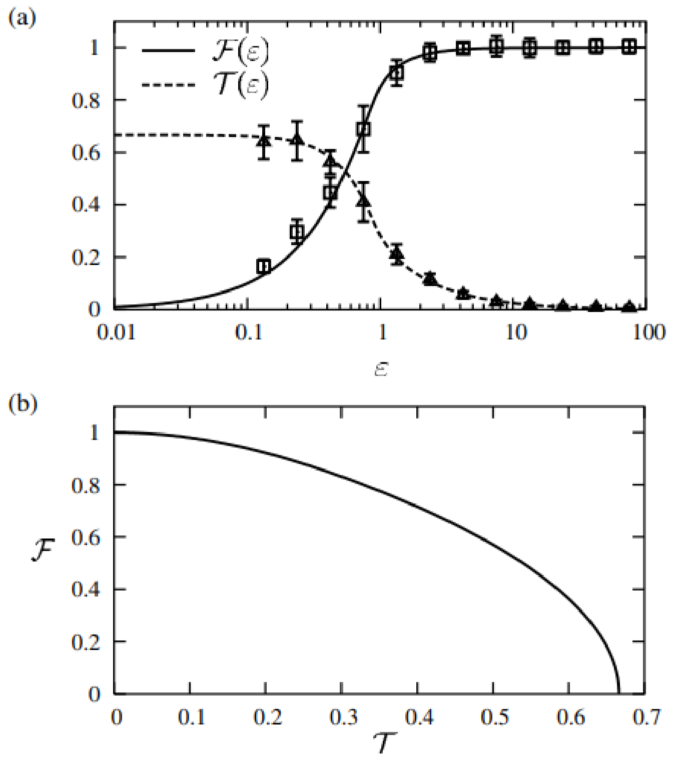

Figure 13: (a) Friction force $\mathcal{F}$ and friction torque $\mathcal{T}$ as a function of ε. (b) Admissible coupling $(\mathcal{F}, \mathcal{T})$. Figure reproduced from [2].

It is observed that the model shows good agreement with the experimental data.

3.3.2 Implementation of the model

Non-dimensionalization

In the numerical implementation, the friction laws are regularized by hyperbolic tangent functions:

$$m\frac{dv}{dt} = -\mu_s mg\,\mathcal{F}(\varepsilon)\tanh\left(\frac{v}{v_d}\right) \tag{52}$$

$$I\frac{d\omega}{dt} = -\mu_s mgR\,\mathcal{T}(\varepsilon)\tanh\left(\frac{\omega R}{v_d}\right) \tag{53}$$

with

$$\varepsilon = \frac{|v|}{R|\omega|} \tag{54}$$

In order to reduce the number of parameters and optimize the numerical resolution, the equations are non-dimensionalized.

The following characteristic quantities are introduced:

$$V_0 = v_0 \tag{55}$$

$$T_0 = \frac{V_0}{\mu_s g} \qquad \text{(this choice simplifies the translational equation of motion)} \tag{56}$$

$$\Omega_0 = \frac{1}{T_0} \tag{57}$$

The dimensionless variables are defined by

$$\tau = \frac{t}{T_0} \tag{58}$$

$$\tilde{v} = \frac{v}{V_0} \tag{59}$$

$$\tilde{\omega} = \frac{\omega}{\Omega_0} \tag{60}$$

The time derivatives then become

$$\frac{dv}{dt} = \frac{V_0}{T_0}\frac{d\tilde{v}}{d\tau} \tag{61}$$

$$\frac{d\omega}{dt} = \frac{\Omega_0}{T_0}\frac{d\tilde{\omega}}{d\tau} \tag{62}$$

The dimensionless regularization parameter is also introduced:

$$\tilde{v}_d = \frac{v_d}{V_0} \tag{63}$$

The parameter ε becomes

$$\varepsilon = \frac{|v|}{R|\omega|} \tag{64}$$

$$= \frac{V_0|\tilde{v}|}{R\Omega_0|\tilde{\omega}|} \tag{65}$$

$$= \gamma\frac{|\tilde{v}|}{|\tilde{\omega}|} \tag{66}$$

with

$$\gamma = \frac{V_0^2}{\mu_s g R}. \tag{67}$$

By substituting these relations into the equations of motion, the dimensionless translational equation is obtained:

$$\frac{d\tilde{v}}{d\tau} = -\mathcal{F}(\varepsilon)\tanh\left(\frac{\tilde{v}}{\tilde{v}_d}\right) \tag{68}$$

For the rotation, one obtains:

$$\frac{1}{T_0^2}\frac{d\tilde{\omega}}{d\tau} = -\frac{\mu_s m g R}{I}\mathcal{T}(\varepsilon)\ \tanh\left(\frac{\tilde{\omega}}{\gamma\tilde{v}_d}\right) \tag{69}$$

$$\frac{d\tilde{\omega}}{d\tau} = -\frac{V_0^2}{\mu_s^2 g^2}\frac{\mu_s m g R}{\frac{1}{2}mR^2}\mathcal{T}(\varepsilon)\ \tanh\left(\frac{\tilde{\omega}}{\gamma\tilde{v}_d}\right) \tag{70}$$

$$\frac{d\tilde{\omega}}{d\tau} = -\frac{2V_0}{\mu_s g R}\mathcal{T}(\varepsilon)\ \tanh\left(\frac{\tilde{\omega}}{\gamma\tilde{v}_d}\right) \tag{71}$$

The final dimensionless system is therefore written as:

$$\begin{cases} \dfrac{d\tilde{v}}{d\tau} = -\mathcal{F}(\varepsilon)\tanh\left(\dfrac{\tilde{v}}{\tilde{v}_d}\right) \\ \dfrac{d\tilde{\omega}}{d\tau} = -2\gamma\mathcal{T}(\varepsilon)\tanh\left(\dfrac{\gamma\tilde{\omega}}{\tilde{v}_d}\right) \end{cases} \tag{72}$$

with

$$\varepsilon = \gamma\frac{|\tilde{v}|}{|\tilde{\omega}|}. \tag{73}$$

The dimensionless initial conditions become

$$\tilde{v}(0) = 1 \tag{74}$$

$$\tilde{\omega}(0) = \frac{\omega_0}{\Omega_0}. \tag{75}$$

Remark on another choice of scales. Another possible choice consists in taking:

$$\Omega_0 = \omega_0 \tag{76}$$

$$T_0 = \sqrt{\frac{R}{2\mu_s g}} \qquad \text{(this choice simplifies the rotational equation of motion)} \tag{77}$$

If v_0 or ω_0 are close to 0, their respective choice of non-dimensionalization is no longer relevant. Knowing that the case $\omega_0 = 0$ is more plausible, the first choice of non-dimensionalization explained here is more appropriate.

Numerical results

First, in order to verify the implementation of the functions $\mathcal{F}(\varepsilon)$ and $\mathcal{T}(\varepsilon)$, [2] indicates the following values:

$$\mathcal{F}(0) = 0, \qquad \lim_{\varepsilon \to \infty} \mathcal{F}(\varepsilon) = 1, \qquad \mathcal{F}(1) = \frac{8}{3\pi}, \qquad \mathcal{F}'(1) = \frac{4}{3\pi}, \tag{78}$$

$$\mathcal{T}(0) = \frac{2}{3}, \qquad \lim_{\varepsilon \to \infty} \mathcal{T}(\varepsilon) = 0, \qquad \mathcal{T}(1) = \frac{8}{9\pi}, \qquad \mathcal{T}'(1) = -\frac{4}{3\pi}. \tag{79}$$

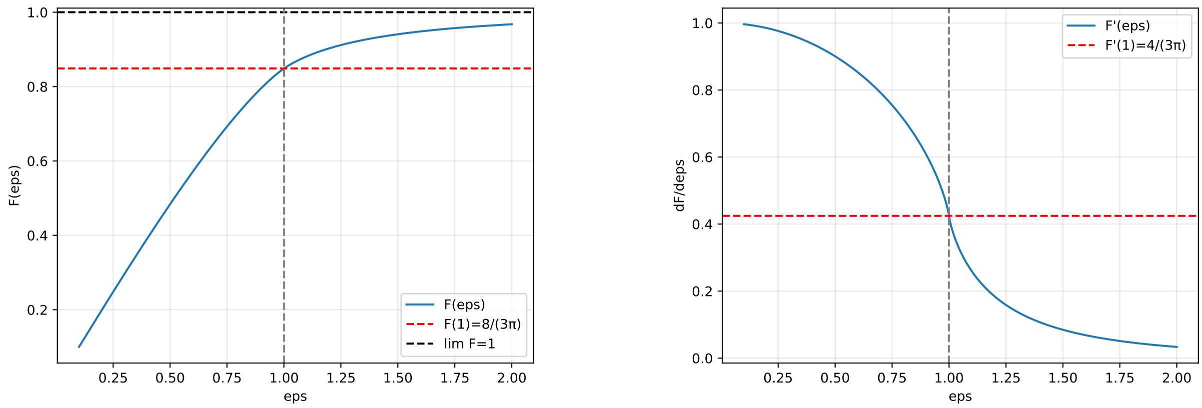

(a) Function $\mathcal{F}(\varepsilon)$. (b) Derivative $\mathcal{F}'(\varepsilon)$.

Figure 14: Numerical validation of $\mathcal{F}$ and its derivative.

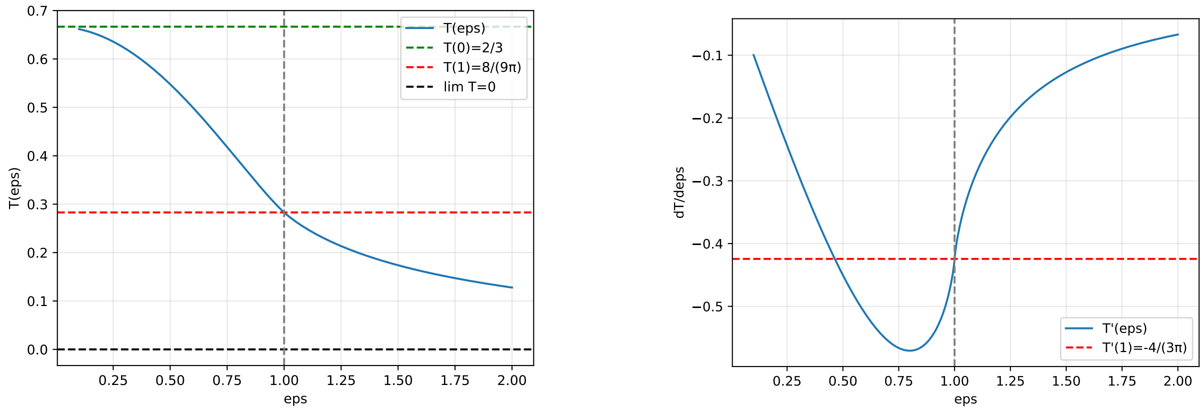

(a) Function $\mathcal{T}(\varepsilon)$. (b) Derivative $\mathcal{T}'(\varepsilon)$.

Figure 15: Numerical validation of $\mathcal{T}$ and its derivative.

As can be observed in Figs. 14 and 15, the results for $\mathcal{F}$, $\mathcal{T}$ and their derivatives are consistent with the expected values.

Then, the same graphs as those of [2] are computed in order to verify the agreement:

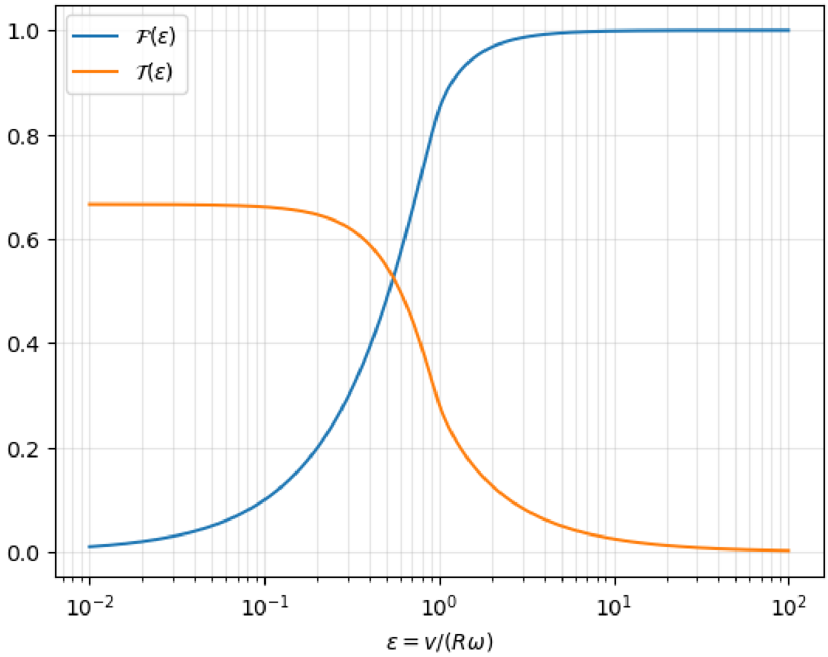

Figure 16: Evolution of $\mathcal{F}(\varepsilon)$ and $\mathcal{T}(\varepsilon)$ as a function of ε.

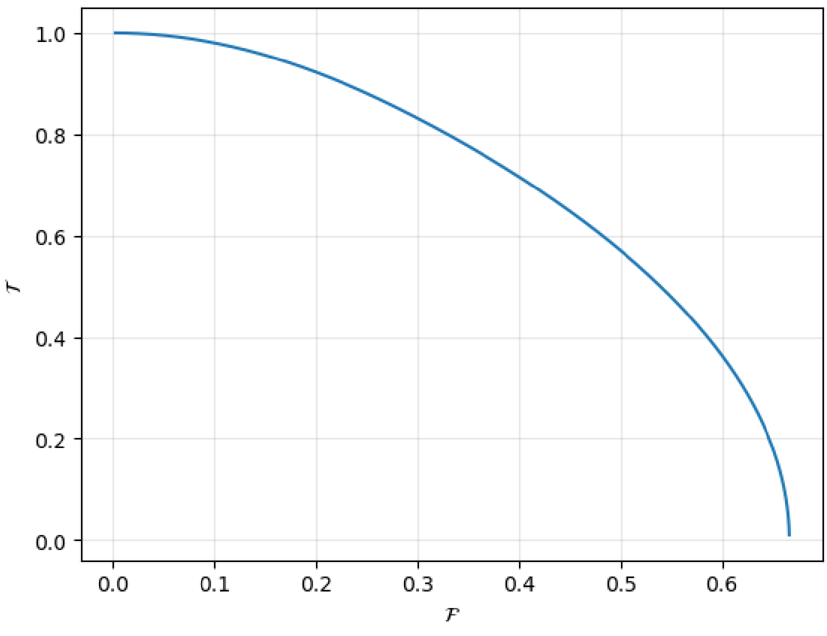

Figure 17: Admissible curve $(\mathcal{F}, \mathcal{T})$.

It is observed in Figs. 16 and 17 that the results correspond to those of the article.

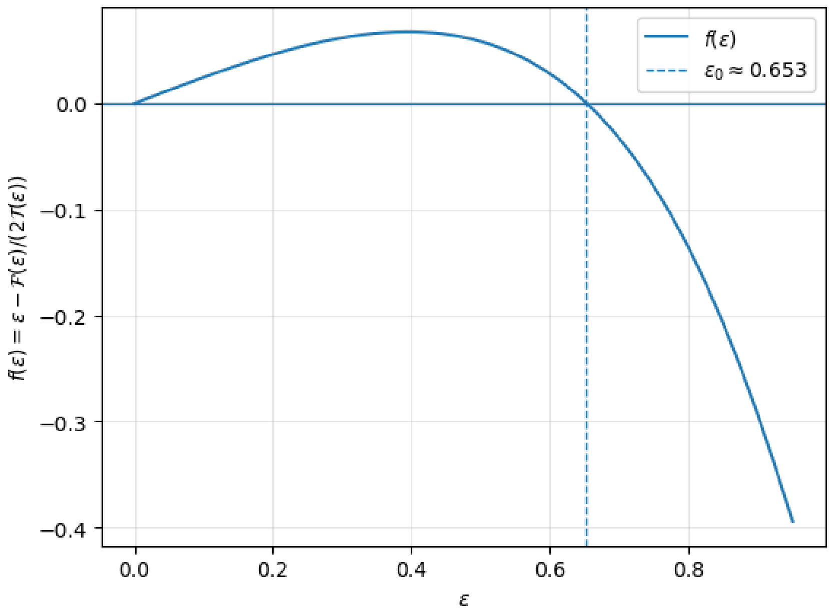

Figure 18: Numerical reproduction of the function $f(\varepsilon)$ introduced by Farkas [2].

Finally, a test case is considered in order to verify that the translational and rotational velocities vanish at the same time (for fixed parameters):

$$V_0 = v_0 = 1, \tag{80}$$

$$T_0 = \frac{V_0}{\mu_s g} = 0.1, \tag{81}$$

$$\gamma = \frac{V_0^2}{\mu_s g R} = 0.1, \tag{82}$$

$$L_0 = V_0 T_0, \tag{83}$$

$$\Omega_0 = \frac{V_0}{R}. \tag{84}$$

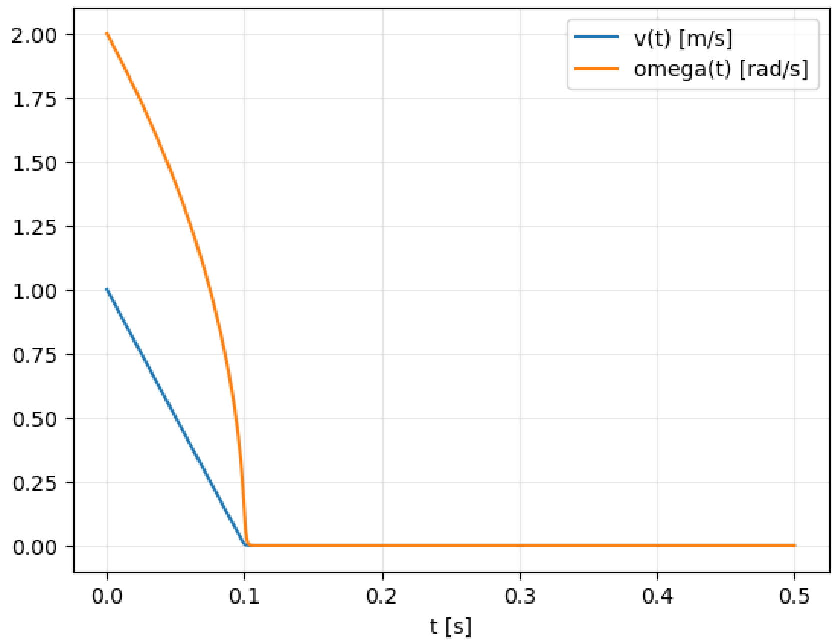

Figure 19: Test case.

The expected result is indeed observed.

4 Impact model

This section presents the impact law used to update the translational and rotational velocities of the NES and the Host at contact. This law is based on the impact model proposed by Luding [18], which accounts for normal restitution, tangential restitution and friction during the collision.

4.1 Description of the model

The moment of inertia of each object is written as

$$I_{N,H} = qmR^2, \tag{85}$$

$$\tag{86}$$

The normal direction at contact is defined by

$$\mathbf{n}_c = \frac{\mathbf{r}_N - \mathbf{r}_H}{\|\mathbf{r}_N - \mathbf{r}_H\|}. \tag{87}$$

The relative velocity at the contact point before impact is

$$\dot{\mathbf{U}}_c^- = \dot{\mathbf{U}}_N^- - \dot{\mathbf{U}}_H^- + \left(R_N\dot{\theta}_N^- - R_H\dot{\theta}_H^-\right)\mathbf{e}_\theta. \tag{88}$$

Its normal and tangential components are

$$\dot{\mathbf{U}}_r^- = \left(\dot{\mathbf{U}}_c^- \cdot \mathbf{e}_r\right)\mathbf{e}_r, \tag{89}$$

$$\dot{\mathbf{U}}_\theta^- = \left(\dot{\mathbf{U}}_c^- \cdot \mathbf{e}_\theta\right)\mathbf{e}_\theta. \tag{90}$$

After impact, the relative velocity becomes

$$\dot{\mathbf{U}}_c^+ = -\varepsilon\dot{\mathbf{U}}_r^- - \beta\dot{\mathbf{U}}_\theta^-. \tag{91}$$

The restitution coefficients satisfy

$$0 \le \varepsilon \le 1, \qquad -1 \le \beta \le 1, \tag{92}$$

$$\varepsilon = \text{const}, \qquad \beta = \min(\beta_0, \beta_1), \qquad \mu_\text{c} = \text{const}. \tag{93}$$

For rolling and sliding contact, the tangential restitution coefficient is given by

$$\text{rolling contact:} \qquad \beta_0 = \text{const}, \tag{94}$$

$$\text{sliding contact:} \qquad \beta_1 = -1 + \mu_\text{c}(1+\varepsilon)\left(1 + q_{NH}^{-1}\right)\frac{\left\|\dot{\mathbf{U}}_r^-\right\|}{\left\|\dot{\mathbf{U}}_\theta^-\right\|}. \tag{95}$$

The reduced inertia terms are defined as

$$
\begin{aligned}
q_{NH}^{-1} &= M_{NH}\left[(q_N M_N)^{-1} + (q_H M_H)^{-1}\right], && (96)\\
M_{NH}^{-1} &= M_N^{-1} + M_H^{-1}. && (97)
\end{aligned}
$$

In the case of a large mass contrast,

$$
\begin{aligned}
M_H &\gg M_N, && (98)\\
q_{NH} &\simeq q_N. && (99)
\end{aligned}
$$

The incident angle is related to the normal-to-tangential velocity ratio by

$$
\frac{\left\|\dot{\mathbf{U}}_r^-\right\|}{\left\|\dot{\mathbf{U}}_\theta^-\right\|} = \cot(\gamma). \tag{100}
$$

The translational velocities after impact are

$$
\dot{\mathbf{U}}_{N,H}^+ = \dot{\mathbf{U}}_{N,H}^- \pm \frac{1}{M_{N,H}}\Delta\mathbf{P}. \tag{101}
$$

The angular velocities after impact are

$$
\dot{\theta}_{N,H}^+ = \dot{\theta}_{N,H}^- \pm \frac{R_{N,H}}{I_{N,H}}\left(\mathbf{e}_r \times \Delta\mathbf{P}\right). \tag{102}
$$

The impulse exchanged during the collision is

$$
\begin{aligned}
\Delta\mathbf{P} &= \int \mathbf{F}_{H\to N}(t)\,dt, && (103)\\
\Delta\mathbf{P} &= M_N\left(\dot{\mathbf{U}}_N^+ - \dot{\mathbf{U}}_N^-\right), && (104)\\
\Delta\mathbf{P} &= -M_H\left(\dot{\mathbf{U}}_H^+ - \dot{\mathbf{U}}_H^-\right). && (105)
\end{aligned}
$$

The contact forces satisfy

$$
\mathbf{F}_{H\to N} = -\mathbf{F}_{N\to H}. \tag{106}
$$

The impulse can then be expressed as

$$
\Delta\mathbf{P} = -M_{NH}(1+\varepsilon)\dot{\mathbf{U}}_r^- - \frac{M_{NH}}{1+q_{NH}^{-1}}(1+\beta)\dot{\mathbf{U}}_\theta^-. \tag{107}
$$

Test 1

In this test, the friction and tangential restitution coefficients are considered with non-zero values. The internal mass is released with a positive then negative rotational velocity and without translational velocity. The internal mass is expected to move to the left after the first rebound when the initial rotational velocity is positive, and to the right when it is negative. Moreover, the trajectories in these two situations are expected to be symmetric.

Table 4: Simulation parameters for the initial rotation symmetry test.

Parameter	**Value**
Friction coefficient μ_c	0.2
Restitution coefficient ε	0.8
Tangential restitution β_0	0.5
Initial state $\mathbf{y}_0$	$(U_{N,x}, U_{N,y}, \dot{U}_{N,x}, \dot{U}_{N,y}, \theta_N, \dot{\theta}_N, U_{H,x}, U_{H,y}, \dot{U}_{H,x}, \dot{U}_{H,y}, \theta_H, \dot{\theta}_H)$
Values	$(0, 0, 0, 0, 0, \pm 5,\ 0, 0, 0, 0, 0, 0)$

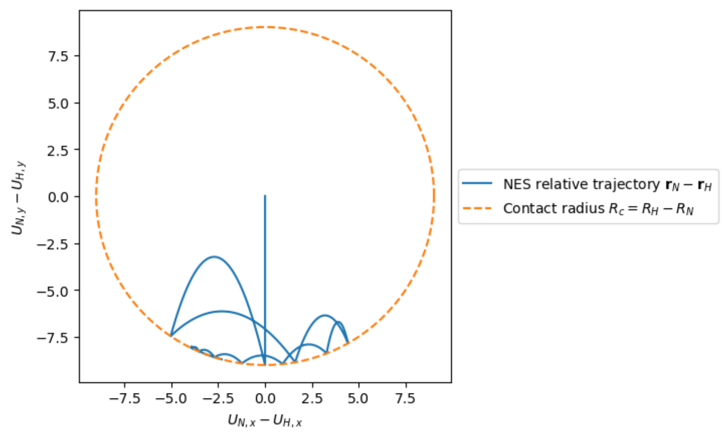

(a) Positive initial angular velocity, $\dot{\theta}_0 = 5$

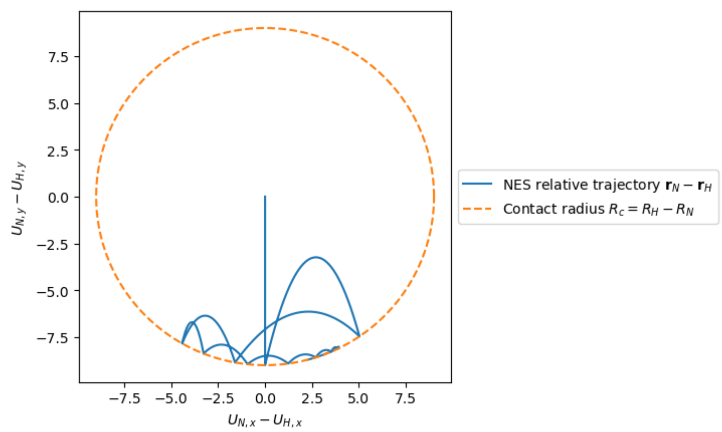

(b) Negative initial angular velocity, $\dot{\theta}_0 = -5$

Figure 20: Initial rotation test: comparison of the NES trajectories for opposite initial angular velocities.

Figure 20 compares the NES trajectories obtained for opposite initial angular velocities. As expected, the two trajectories are symmetric with respect to the vertical axis, and the direction of motion after the first rebound is reversed when the sign of the initial angular velocity is changed.

4.1.1 Energy tests

In this new series of tests, a container with a very large mass is still considered so that it remains practically motionless. This time, tests on the energy of the system are performed.

Test 1

In this first test, the internal mass is again released without initial velocity from the center of the container with a restitution coefficient $\varepsilon = 1$. The total energy is expected to remain constant, while only transfers between the kinetic and potential energies of the internal mass are expected.

Table 5: Simulation parameters for the conservative energy test with $\varepsilon = 1$.

Parameter	**Value**
Friction coefficient μ_c	0
Restitution coefficient ε	1
Tangential restitution β_0	0
Initial state $\mathbf{y}_0$	$(0, 0, 0, 0, 0, 0,\ 0, 0, 0, 0, 0, 0)$

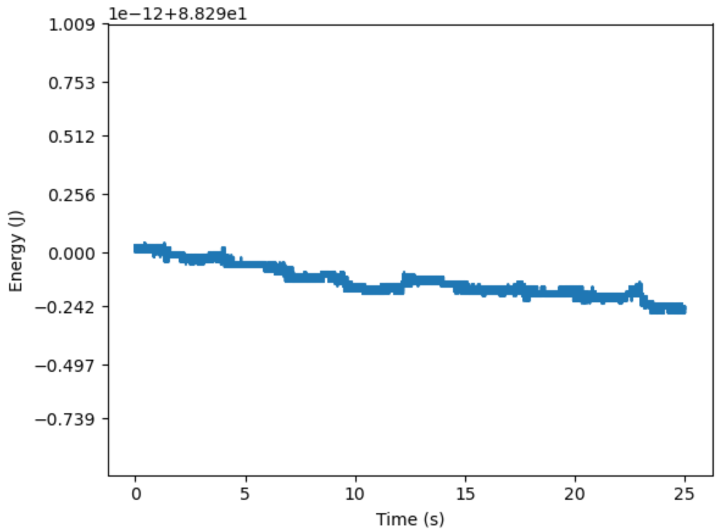

(a) Total mechanical energy

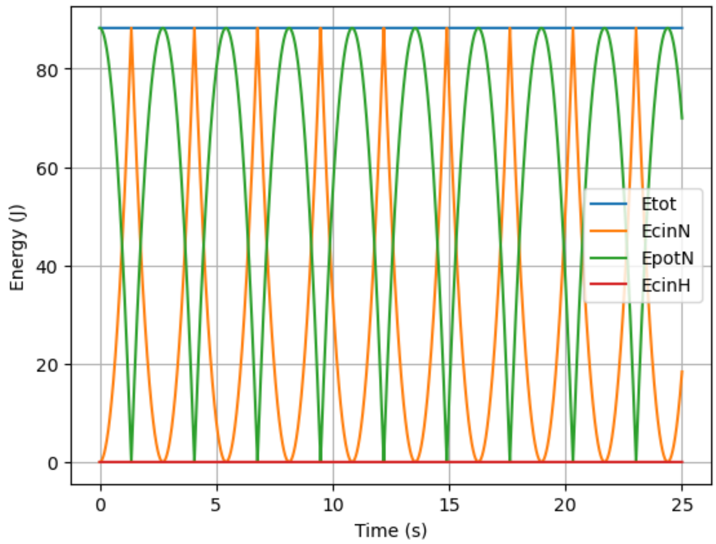

(b) Kinetic and potential energies

Figure 21: Energy conservation test with $\varepsilon = 1$: total, kinetic and potential energies over time.

Figure 21 shows the evolution of the total, kinetic and potential energies for the conservative case. The expected behavior is observed: the total mechanical energy remains constant, while energy is exchanged between kinetic and potential forms. The variations in the total energy are of the order of 10^{-12}, which is negligible.

Test 2

The same situation as in the previous test is considered, but with a restitution coefficient $\varepsilon = 0.9$. At each rebound, the total energy is expected to decrease, so that the graph follows a staircase-shaped curve.

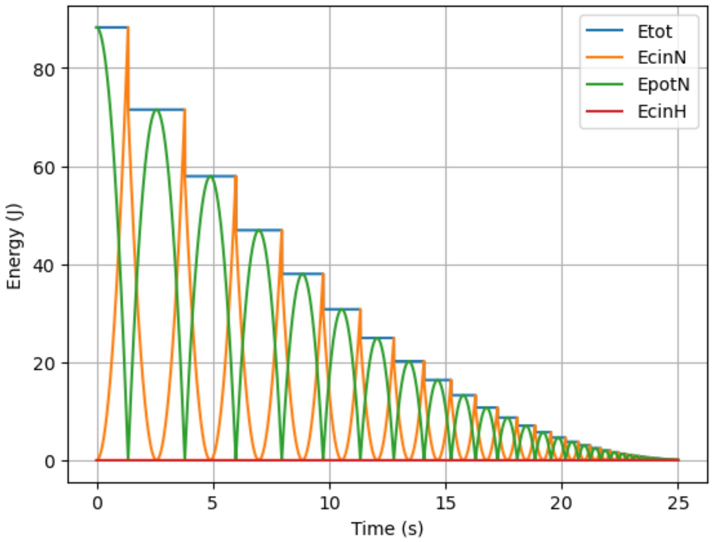

Figure 22: Energy dissipation test with $\varepsilon = 0.9$: decrease of the total energy after successive impacts.

Table 6: Simulation parameters for the dissipative energy test with $\varepsilon = 0.9$.

Parameter	**Value**
Friction coefficient μ_c	0
Restitution coefficient ε	0.9
Tangential restitution β_0	0
Initial state $\mathbf{y}_0$	$(0, 0, 0, 0, 0, 0,\ 0, 0, 0, 0, 0, 0)$

Figure 22 shows the energy evolution for the dissipative case. As expected, the total mechanical energy decreases after each rebound, leading to a staircase-shaped curve, while the kinetic and potential energies continue to exchange between one another between impacts.

4.1.2 Extreme operating tests

In this new series of tests, various extreme situations are tested in order to determine whether the model remains robust and to detect possible limitations.

For all the following tests, the masses and radii are kept unchanged:

$$R_N = 1, \qquad R_H = 10, \qquad M_N = 1, \qquad M_H = 10^9.$$

Test 1a

In this first test, a very large velocity along the y direction is applied to the internal mass and the result is observed.

Table 7: Simulation parameters for the extreme velocity test along the y direction.

Parameter	Value
Friction coefficient μ_c	0.4
Restitution coefficient ε	0.9
Tangential restitution β_0	0.7
Initial state $\mathbf{y}_0$	$(0, 0, 0, 1200, 0, 0, \ 0, 0, 0, 0, 0, 0)$

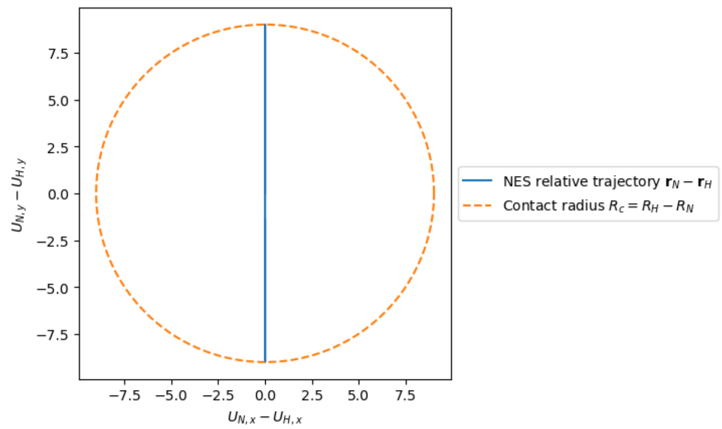

(a) Simulated trajectory

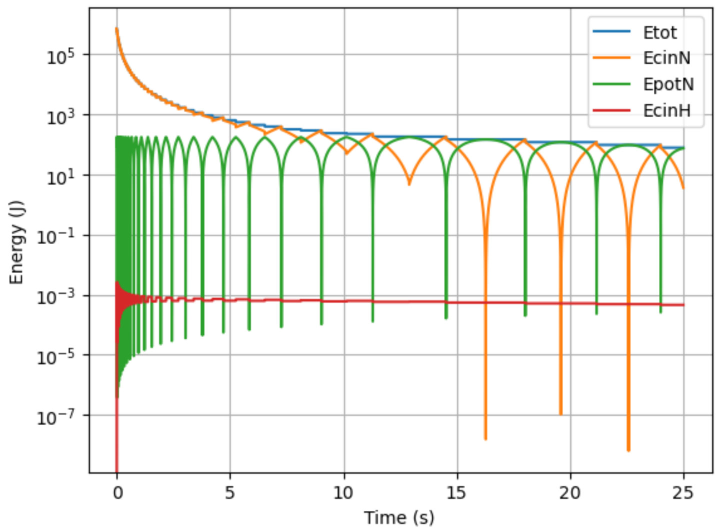

(b) Energy evolution

Figure 23: Extreme velocity test along the y direction: trajectory and energy evolution.

Figure 23 shows the trajectory and energy evolution obtained when a very large initial velocity is applied along the y direction.

Test 1b

The same principle is used as in the previous test, but with a very large initial velocity along the x direction.

Table 8: Simulation parameters for the extreme velocity test along the x direction.

Parameter	**Value**
Friction coefficient μ_c	0.4
Restitution coefficient ε	0.9
Tangential restitution β_0	0.7
Initial state $\mathbf{y}_0$	$(0, 0, 2000, 0, 0, 0,\ 0, 0, 0, 0, 0, 0)$

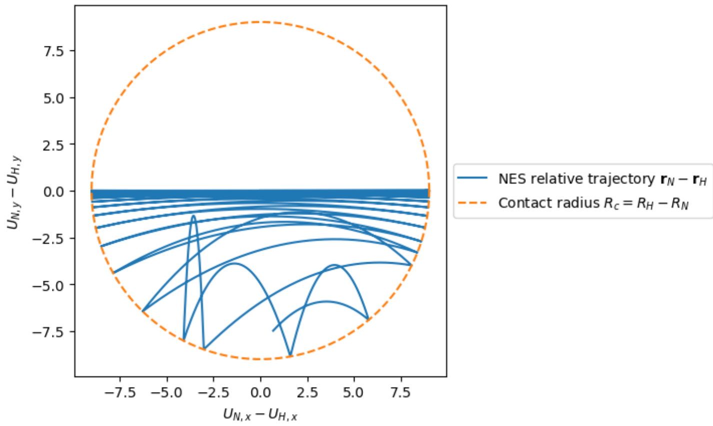

(a) Simulated trajectory

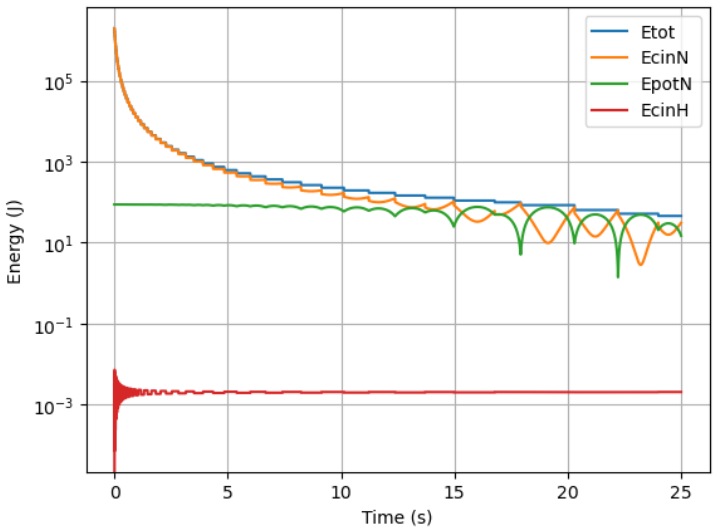

(b) Energy evolution

Figure 24: Extreme velocity test along the x direction: trajectory and energy evolution.

Figure 24 shows the trajectory and energy evolution obtained when a very large initial velocity is applied along the x direction.

Test 2a: Symmetry 1

Here, a symmetry test is performed. The internal mass is released on the right side of the container with velocities along x and y, and a rotational velocity. This mass is then considered at the same position on the left side with an opposite velocity along x and an opposite rotational velocity. The trajectories are expected to be symmetric.

Table 9: Simulation parameters for the first symmetry test.

Parameter	**Value**
Friction coefficient μ_c	0.4
Restitution coefficient ε	0.9
Tangential restitution β_0	0.7
Initial state $\mathbf{y}_0$	$(2, 0, 150, -200, 0, 200, \ 0, 0, 0, 0, 0, 0)$

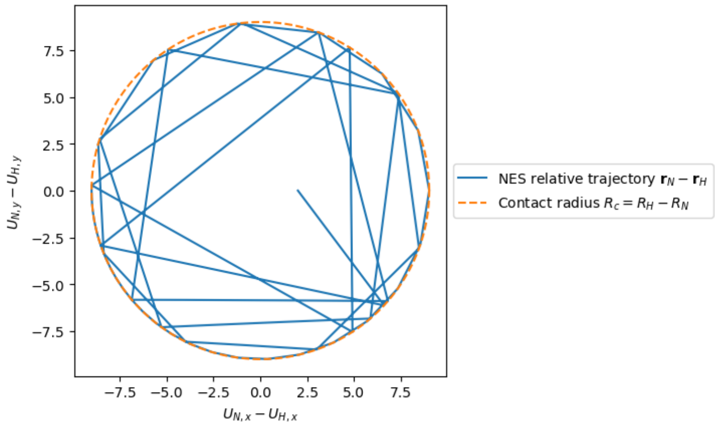

(a) Simulated trajectory

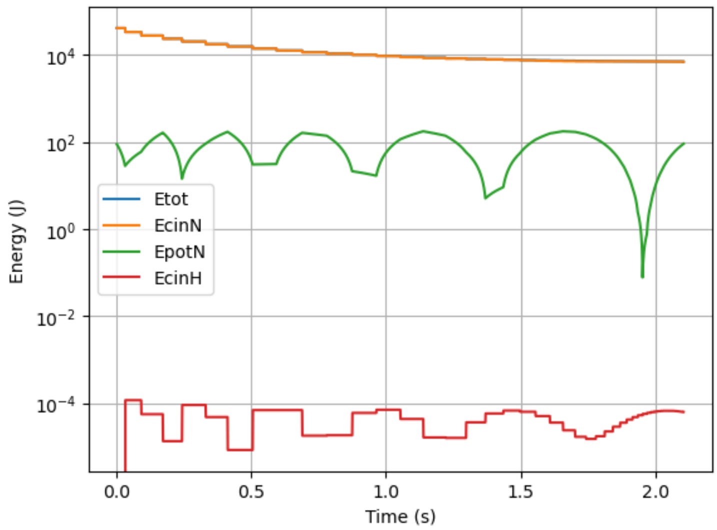

(b) Energy evolution

Figure 25: First symmetry test: trajectory and energy evolution for the reference initial condition.

Figure 25 shows the trajectory and the energy evolution obtained for the reference initial condition.

Test 2b: Symmetry 2

The same test is then repeated using the symmetric initial condition.

Table 10: Simulation parameters for the second symmetry test.

Parameter	Value
Friction coefficient μ_c	0.4
Restitution coefficient ε	0.9
Tangential restitution β_0	0.7
Initial state $\mathbf{y}_0$	$(-2, 0, -150, -200, 0, -200,\ 0, 0, 0, 0, 0, 0)$

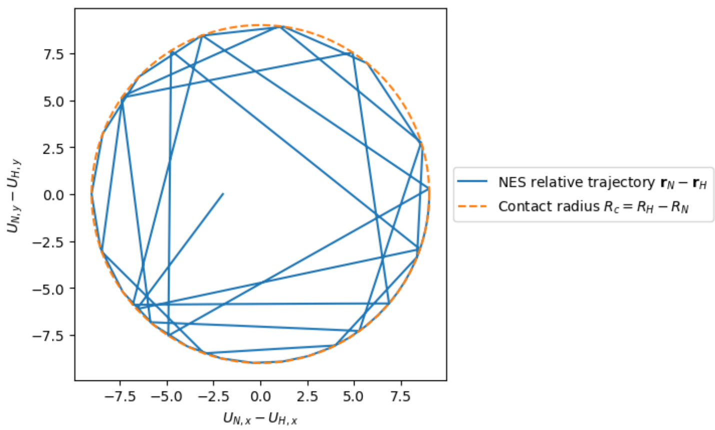

(a) Simulated trajectory

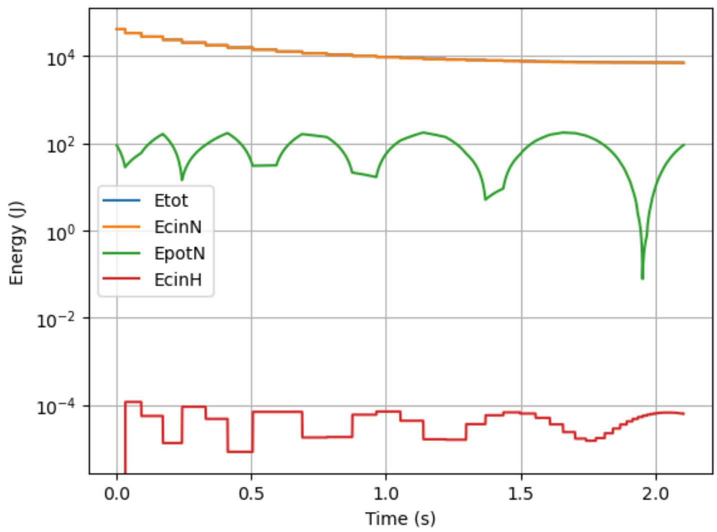

(b) Energy evolution

Figure 26: Second symmetry test: trajectory and energy evolution for the symmetric initial condition.

Figure 26 shows the trajectory and the energy evolution obtained for the symmetric initial condition.

Verification

The symmetry of the two simulations is then verified by comparing the time evolution of the corresponding coordinates.

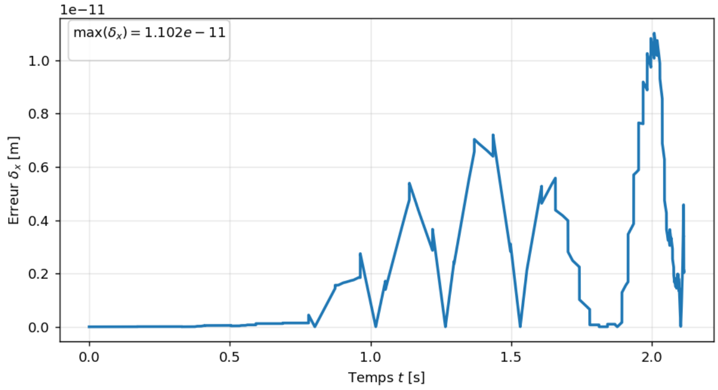

(a) Error $\delta_x(t) = |x_1(t) + x_2(t)|$

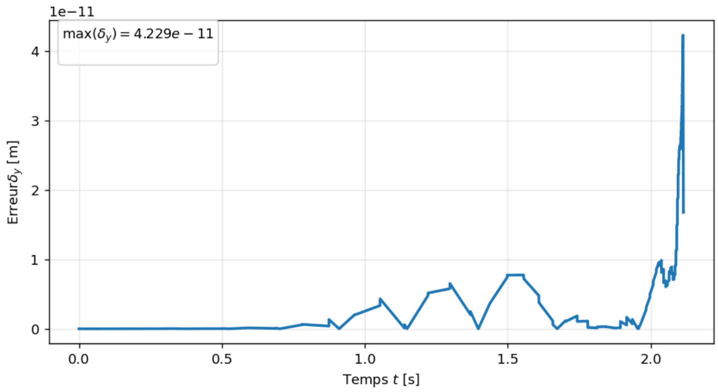

(b) Error $\delta_y(t) = |y_1(t) - y_2(t)|$

Figure 27: Verification of the trajectory symmetry by comparing the x and y coordinates of the two symmetric simulations.

Figure 27 shows the errors used to verify the symmetry of the two trajectories.

Test 3

Here, an internal mass launched very close to the wall and with a high initial velocity is considered.

Table 11: Simulation parameters for the high-velocity test near the container wall.

Parameter	**Value**
Friction coefficient μ_c	0.9
Restitution coefficient ε	0.9
Tangential restitution β_0	-0.5
Initial state $\mathbf{y}_0$	$(0,\ R_c - 10^{-2},\ 1000,\ 0,\ 0,\ 0,\ 0,\ 0,\ 0,\ 0,\ 0,\ 0)$

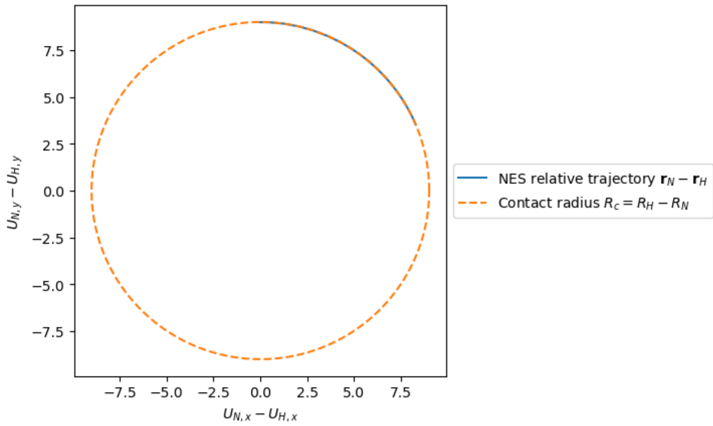

(a) Simulated trajectory

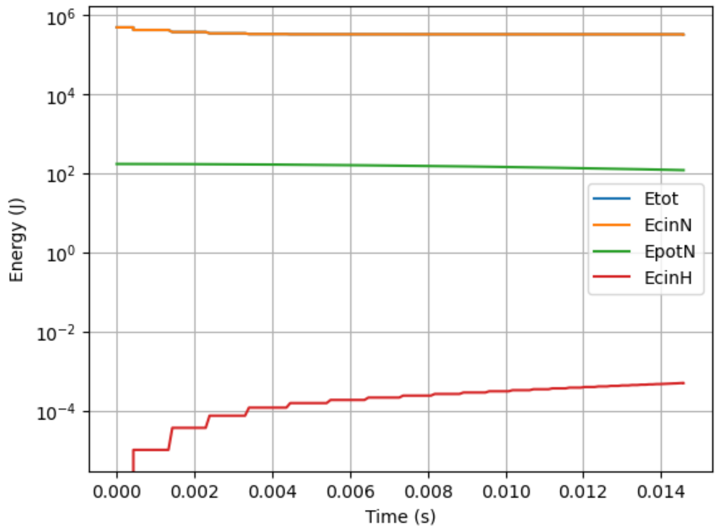

(b) Energy evolution

Figure 28: High-velocity test near the wall: trajectory and energy evolution.

Figure 28 shows the trajectory and the energy evolution obtained when the internal mass is initially placed very close to the wall and launched with a high velocity.

Overall, these extreme operating tests show that the numerical implementation remains stable and gives physically consistent results under severe initial conditions.

4.1.3 Cases where the internal mass exits the container

In some cases, it was observed that the internal mass exited the wall (see Figure 29). This problem is detailed in the following part.

Problem

Table 12: Parameters used in the simulation where the internal mass exits the container.

Parameter	**Value**
R_N	0.01
R_H	10
Contact radius $R_c = R_H - R_N$	9.99
M_N	0.1
M_H	10^9
g	9.81
Friction coefficient μ_c	0.8
Restitution coefficient ε	0.9
Tangential restitution β_0	1.0
Initial state $\mathbf{y}_0$	$(-2, -6, 300, 200.1, 0, 0, 0, 0, 0, 0, 0, 0)$

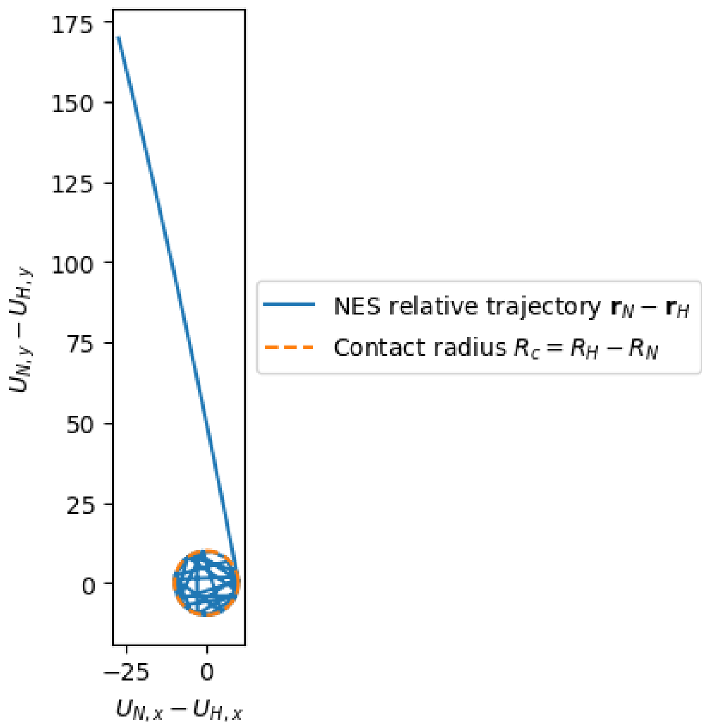

Figure 29: Example of a numerical trajectory where the internal mass exits the container after contact.

Resolution of the problem

Numerically, the internal mass cannot be in contact with the wall with infinite precision. Indeed, when the contact event occurs, the root-finding algorithm of *solve_ivp* locates the contact with an error of the order of machine precision. Thus, approximately one time out of two, the internal mass is located slightly outside the wall. In most cases, at the next iteration, the NES is sent back inside the wall and there is no problem. However, in cases where the velocity of the NES at contact is in the tangential direction, it may not re-enter the wall at the next iteration and may continue its trajectory outside.

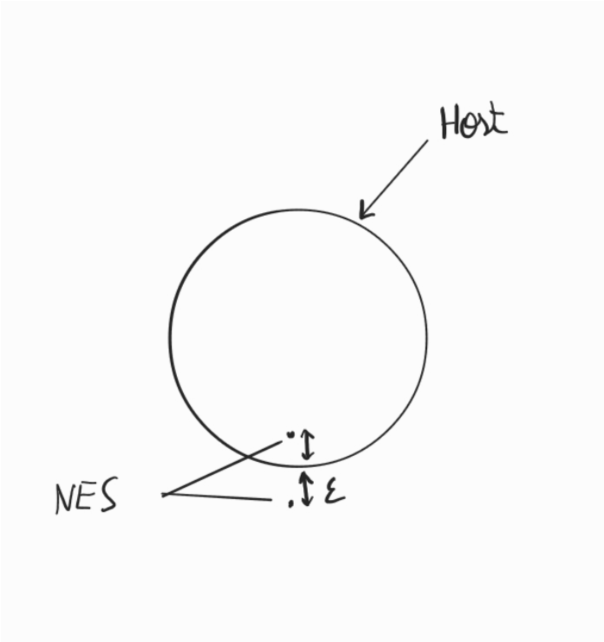

Figure 30: Illustration of the numerical issue occurring when the internal mass is detected slightly outside the wall at contact.

To remedy this problem, at each contact, it will be checked whether the NES is located inside or outside, and if it is outside: reintegrate with *solve_ivp* backwards until the previous time step. By proceeding in this way, the NES is indeed located inside. However, a condition must still be added to control the distance between the NES and the wall. Thus, a tolerance will be imposed (for example 10^{-13}), and as long as this tolerance is not satisfied, the backward time interval of *solve_ivp* will be divided by two, while imposing that the internal mass must be on the inner side of the wall.

5 Additional numerical configurations

This section presents two additional numerical configurations used to further investigate the OVINES dynamics. The first one considers a Host connected to the ground by springs and dampers, while the second one qualitatively studies the influence of friction on the NES motion.

5.1 Host connected to the ground by springs and dampers

After the validation of the simplified OVINES model, a more complete configuration is considered. In this case, the Host is no longer fixed, but is connected to the ground by translational and rotational springs and dampers. The system therefore includes three degrees of freedom for the Host: two translations and one rotation. The NES is modeled as a disk moving inside the circular Host and impacting the inner wall.

The objective of this simulation is to observe the behavior of the coupled Host–NES system when the Host is subjected to a harmonic ground excitation. The parameters and initial conditions used for the simulation are summarized in Table 13.

Parameter	Symbol	Value	Unit
System parameters			
Mass ratio	$\hat{m} = M_N/M_H$	0.2	–
NES radius ratio	$\hat{R}_N = R_N/L_{\text{ref}}$	0.2	–
Container radius ratio	$\hat{R}_H = R_H/L_{\text{ref}}$	1.0	–
NES inertia coefficient	q_N	1.0	–
Container inertia coeff.	q_H	1.0	–
Oscillator parameters			
Damping ratio (translation)	ξ	0.02	–
Damping ratio (rotation)	ξ_θ	0.02	–
Frequency ratio (y/x)	$\hat{c}$	1.0	–
Stiffness ratio (y/x)	$\hat{k}$	1.0	–
Rotational frequency ratio	$\hat{\omega}$	1.0	–
Excitation amplitude (x)	$\hat{A}_x$	0.0	–
Excitation amplitude (y)	$\hat{A}_y$	0.005	–
Impact law			
Restitution coefficient	ε	0.97	–
Tangential restitution	β_0	0.5	–
Friction coefficient	μ_{c}	0.0	–
Reference values			
Reference length	L_{ref}	1.0	m
Container mass	M_H	1.0	kg
Excitation frequency	ω	1.0	rad/s
Simulation duration	τ_f	2000	–
Initial conditions			
N position	$(x_N^0,\, y_N^0)$	$0.99\, R_c\, (\cos 315^\circ,\, \sin 315^\circ)$	m
N velocity	$(\dot{x}_N^0,\, \dot{y}_N^0)$	(0, 0)	m/s
N angle & ang. vel.	$(\theta_N^0,\, \dot{\theta}_N^0)$	(0, 0)	rad, rad/s
H position	$(x_H^0,\, y_H^0)$	(0, 0)	m
H velocity	$(\dot{x}_H^0,\, \dot{y}_H^0)$	(0, 0)	m/s
H angle & ang. vel.	$(\theta_H^0,\, \dot{\theta}_H^0)$	(0, 0)	rad, rad/s

Table 13: Dimensionless parameters and initial conditions used in the simulation.

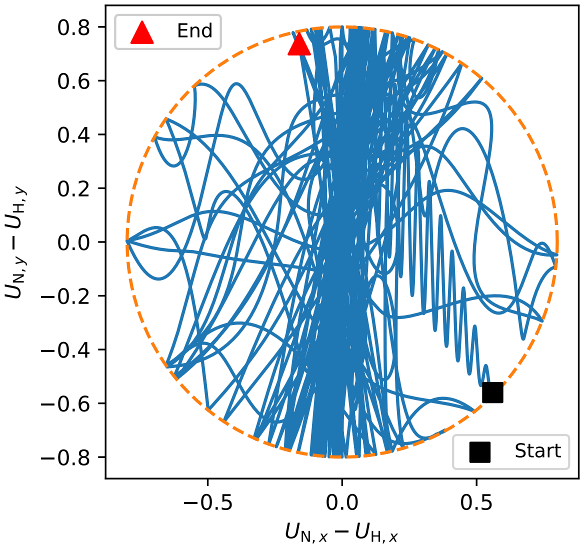

Figure 31: Relative trajectory of the NES inside the moving Host connected to the ground by springs and dampers.

Figure 31 shows the relative trajectory of the NES inside the moving Host. The dashed circle represents the theoretical contact boundary, corresponding to the radius $R_c = R_H - R_N$. The trajectory shows that the NES undergoes multiple impacts with the Host wall and that its motion is not restricted to the direction of excitation.

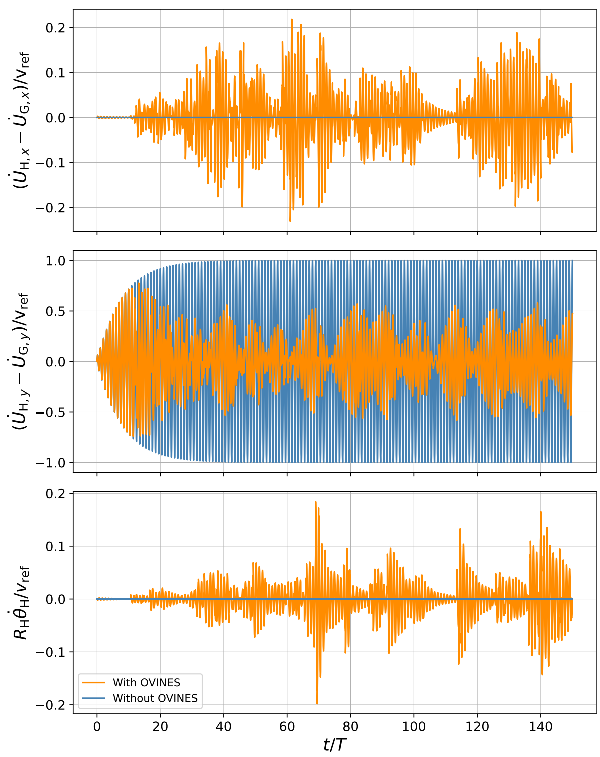

Figure 32: Time evolution of the Host translational and rotational velocities for the ground-connected Host model.

Figure 32 presents the time evolution of the Host velocities. The response of the Host is shown in translation along the x and y directions, as well as in rotation. The results show that the presence of the NES induces a reduction in the amplitude of the Host velocity in the excitation direction. It can also be observed that motions in the other directions appear. The NES therefore seems to induce an energy transfer from the excitation direction toward the other directions.

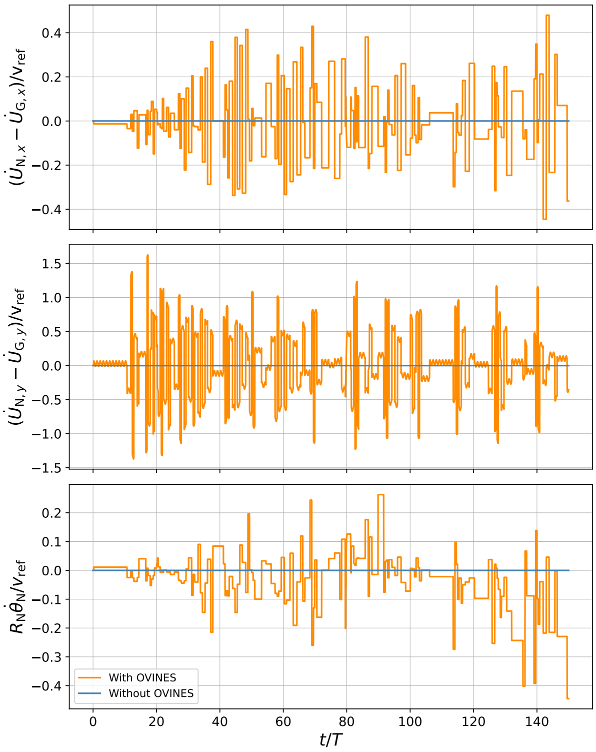

Figure 33: Time evolution of the NES translational and rotational velocities for the ground-connected Host model.

Figure 33 shows the time evolution of the NES coordinates. As can be observed, the impacts between the Host and the NES lead to an increase in the NES velocity components in the three directions, which indicates an energy transfer from the Host to the NES.

Overall, this configuration shows that the successive impacts transfer part of the energy from the Host to the NES and also redistribute the motion among the translational and rotational degrees of freedom.

5.2 Qualitative influence of friction on the NES motion

In the previous section, the Host was connected to the ground by springs and dampers, and its response resulted from the coupled dynamics of the primary structure and the NES. In the present section, a simpler configuration is considered in order to focus specifically on the influence of friction. The Host motion is directly imposed by a harmonic excitation in the vertical direction, without modelling the springs and dampers of the primary structure.

Two simulations are compared. In both cases, the same initial conditions and excitation parameters are used. The only difference lies in the friction coefficients.

Table 14: Common parameters and initial conditions used for the friction influence study.

Parameter	**Symbol**	**Value**
Excitation frequency	f	11 Hz
Angular frequency	ω	$2\pi f$
Shaker acceleration	a_{PV}	$-9g$
Excitation amplitude	A	-1.85×10^{-2} m
Host radius	R_H	0.10 m
NES radius	R_N	0.02 m
Contact radius	$R_c = R_H - R_N$	0.08 m
NES mass	M_N	0.003 kg
Host mass	M_H	∞
Normal restitution coefficient	ε	1.0
Tangential restitution coefficient	β_0	1.0
Simulation duration	t_f	1.0 s
Initial NES position	(x_N^0, y_N^0)	$0.98R_c(\cos(-45°), \sin(-45°))$
Initial NES velocity	$(\dot{x}_N^0, \dot{y}_N^0)$	$(0, 0)$
Initial NES rotation	$(\theta_N^0, \dot{\theta}_N^0)$	$(0, 0)$
Initial Host position	(x_H^0, y_H^0)	$(0, 0)$
Initial Host velocity	$(\dot{x}_H^0, \dot{y}_H^0)$	$(0, 0)$
Initial Host rotation	$(\theta_H^0, \dot{\theta}_H^0)$	$(0, 0)$

Table 15: Friction coefficients used in the two compared cases.

Parameter	**Case 1**	**Case 2**
Collision friction coefficient μ_{c}	10^9	0.5
Ground friction coefficient μ_{s}	10^{-9}	0.5

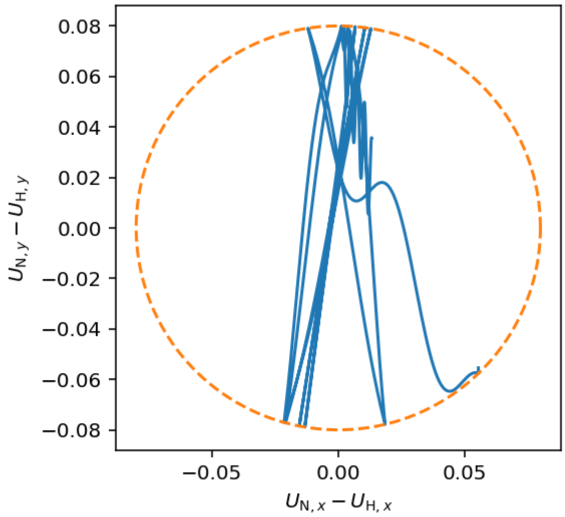

Relative trajectory

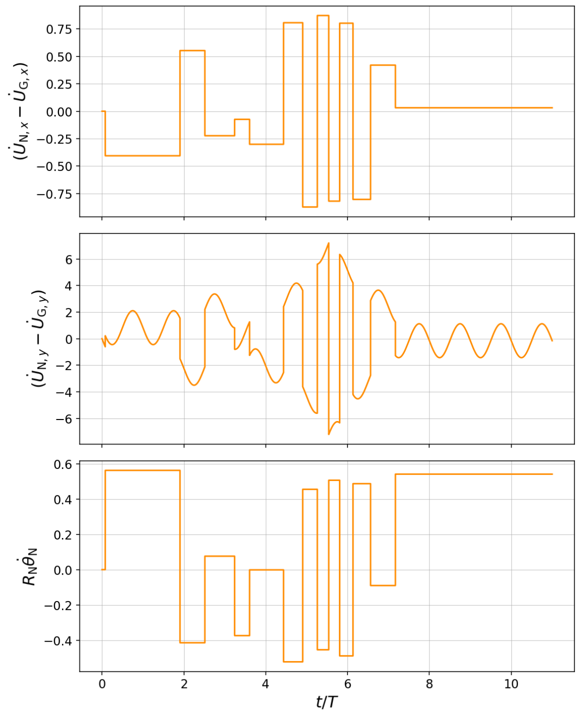

Relative velocities

Figure 34: NES trajectory and relative velocities without frictional energy dissipation.

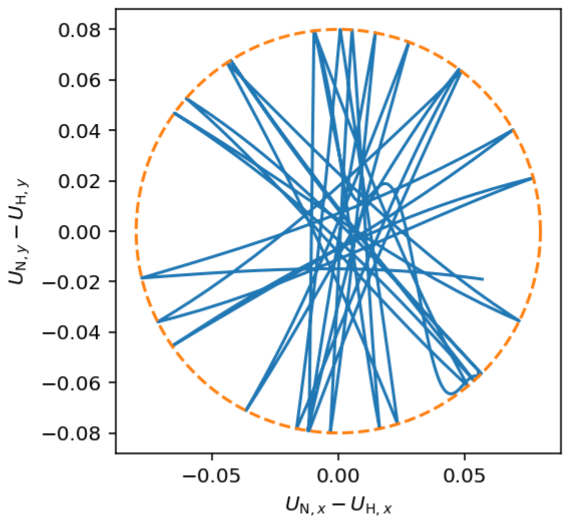

Relative trajectory

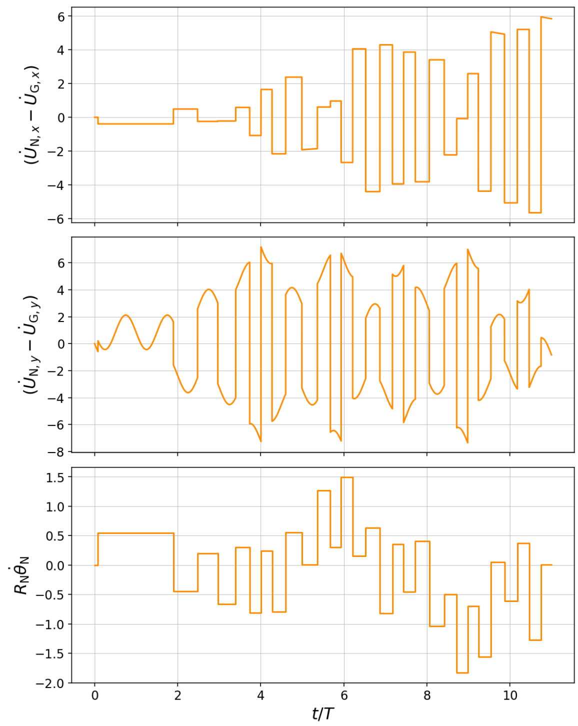

Relative velocities

Figure 35: NES trajectory and relative velocities with frictional energy dissipation.

It can be observed in Figs. 34 and 35 that, for the same simulation duration, the case with frictional energy dissipation counter-intuitively leads to larger NES velocity components in the x and θ directions, as well as to a larger number of rebounds. This suggests that ground friction does not only dissipate energy, but also modifies the sequence of impacts and promotes a redistribution of the NES motion among the translational and rotational directions. However, this observation is only qualitative at this stage and should be investigated further through additional simulations and a more detailed energy analysis.

Part II
Experimental part

This second part focuses on the experimental study of the OVINES system. The objective is to design and test several experimental configurations, reconstruct the motion of the NES and of the Host using a two-camera measurement setup, and perform a first identification of the impact parameters from the reconstructed trajectories.

6 Objectives of the experimental study

In the first part of the report, a numerical OVINES model was implemented. The objective of this part is therefore to experimentally observe the OVINES dynamics and to initiate a first calibration of the numerical model. At the beginning of this section, several questions therefore arise: choice of the materials of the NES and the Host, dimensions of these latter, model parameters to use beforehand. To do this, specifications were taken into account in order to satisfy certain conditions. First of all, a shaker will be used in order to excite the Host, and the latter has the following performances (Fig. 36).

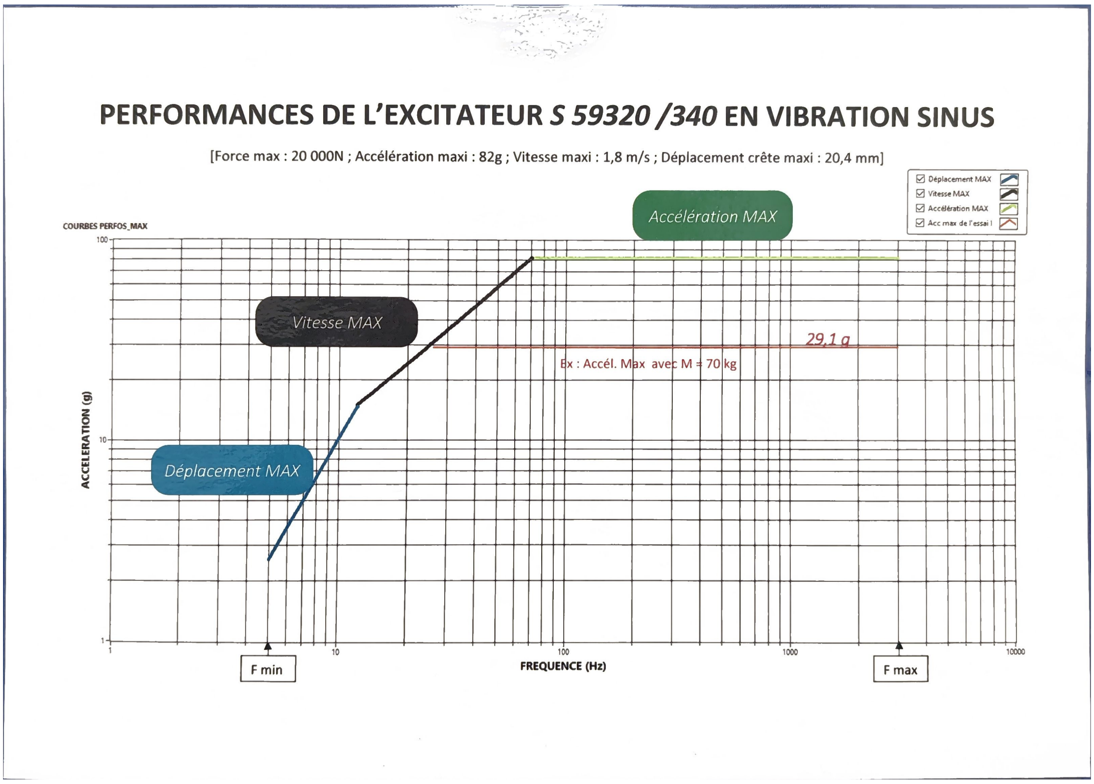

Figure 36: Shaker performance limits.

The acceleration and frequency imposed on the shaker must be located below the 3 curves of Fig. 36.

Also, concerning the amplitude of the excitation to apply to the Host, the article [3] shows the optimal amplitude to apply in the 1D case (Fig. 37). The amplitude of the excitation will be applied around this reference amplitude, which is equal to:

$$A_0 = \frac{L_g}{\pi} \tag{108}$$

with the clearance L_g corresponding to the difference between the diameters of the Host wall and the NES: $L_g = 2R_H - 2R_N$.

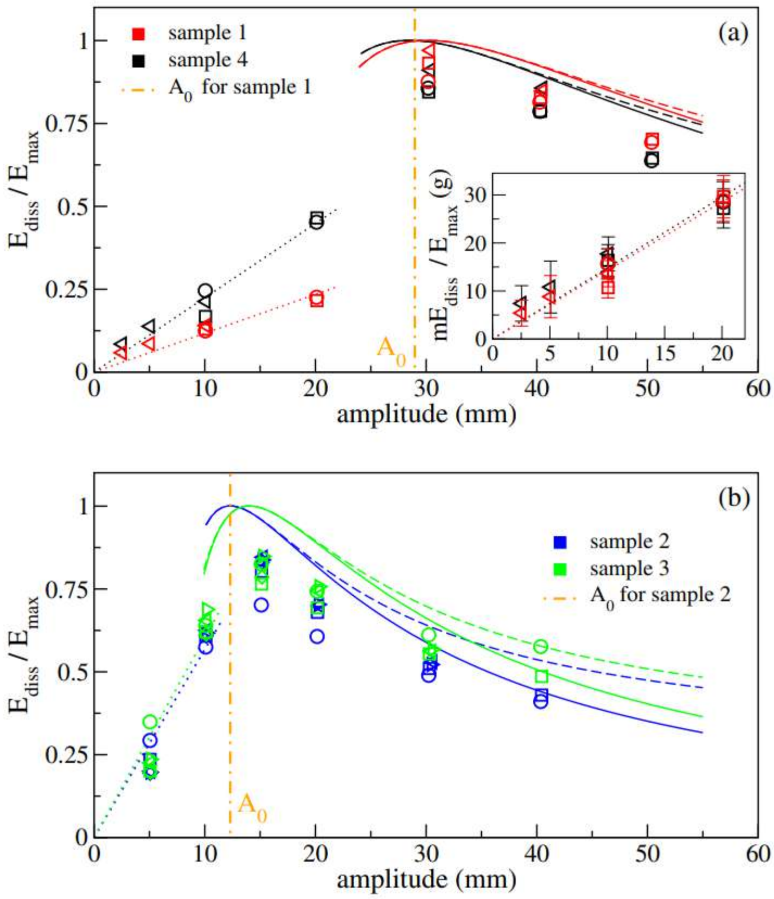

Figure 37: Optimal excitation amplitude for a one-dimensional vibro-impact NES, adapted from [3].

Remark: the maximum amplitude of the shaker is of the order of 2 cm ($\approx$ 1 inch), thus this amplitude A_0 which will be applied must properly satisfy this criterion, which will have an impact on the radii of the Host and NES allowing this optimal amplitude to be applied.

Finally, the ratio of the radii between the NES and the Host will be chosen as 0.2, so that the NES has a notable influence on the Host.

7 Experimental method

This section presents the measurement and post-processing methods used to reconstruct the motion of the OVINES system. It describes the camera calibration procedure, the reconstruction of the Host geometry, the estimation of the NES rotation, the impact detection method and the parameter identification procedure.

7.1 Optical calibration

During the experimental tests with the cameras, it is necessary to carry out a calibration in order to know the parameters necessary for the data processing. Calibration is the recognition process that makes it possible to know the intrinsic and extrinsic parameters of the cameras, necessary to measure the real sizes of the observed objects, remove the distortion effects of the cameras and reposition the positions of the cameras in space.

In order to successfully carry out the calibration, different conditions must be satisfied. A calibration board is necessary, several shapes are possible but in this case a Charuco board will be used for the experiments (Fig. 38); at least 10-15 images are necessary, the board must undergo inclinations and rotations during the acquisitions; the focus and the lighting of the markers must be correct; the dimensions of the marker must be greater than 20 pixels.

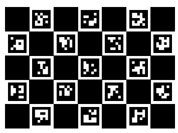

www.calib.io | 5x7 | Checker Size: 8 mm | Marker Size: 6 mm | Dictionary: ArUco DICT_5X5.

Figure 38: ChArUco board used for camera calibration.

Mathematically, the calibration formula is the following:

$$s \begin{bmatrix} u \\ v \\ 1 \end{bmatrix} = K[R\,t] \begin{bmatrix} X \\ Y \\ Z \\ 1 \end{bmatrix} \tag{109}$$

with

- s: scale factor
- u,v: pixel coordinates in the camera
- K: intrinsic matrix

- R, t: extrinsic parameters
- X,Y,Z: coordinates in real space

7.1.1 Intrinsic calibration

The intrinsic calibration is performed independently for each camera.

It is used to determine the internal parameters of the camera, which are contained in the intrinsic matrix K, as well as the distortion coefficients. These parameters are necessary to correct the optical distortion of the cameras.

To do this, several images of the ChArUco board must be captured from different positions and inclinations, typically at least 15 to 20 images.

7.1.2 Extrinsic calibration

The extrinsic calibration is performed to determine the position of the cameras in space with respect to the calibration board. This position is defined using a rotation vector R and a translation vector t. A single image containing the ChArUco board is sufficient to perform the extrinsic calibration.

The calibration parameters are then used, through Eq. 109, to reconstruct the 3D positions of the tracked markers from their 2D image coordinates.

7.2 Post-processing method

This section presents the experimentally acquired measurement results, as well as the post-processing of the data allowing the reconstruction of the trajectory, rotation and velocity of the NES as well as other elements allowing the analysis and the comparison with the numerical model.

7.2.1 Post-processing software

Image processing, camera calibration, as well as the final reconstruction of the marker coordinates in physical units are performed using the open-source software "VibrationTracker", developed by [20]. This software makes it possible to perform actions by blocks, in this case the block branches used for this study are the following (Fig. 39).

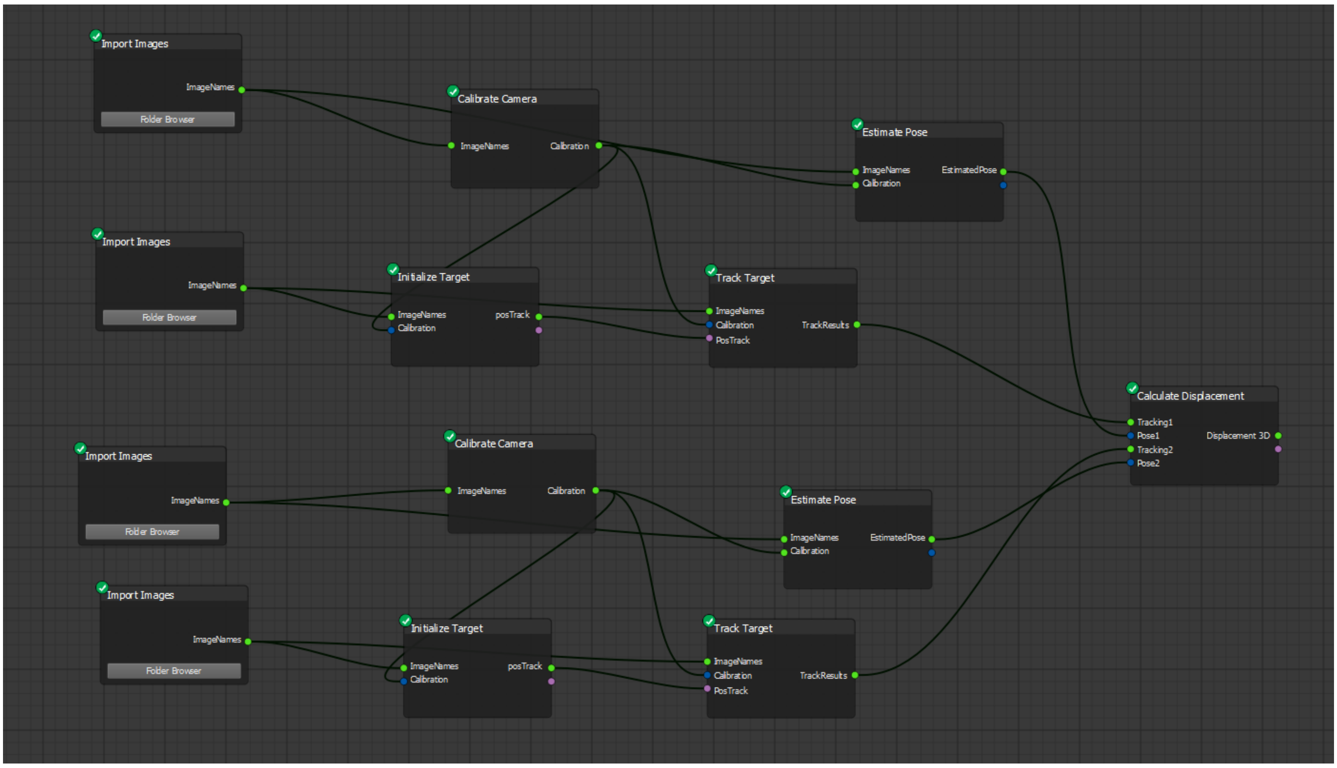

Figure 39: VibrationTracker workflow used for camera calibration, marker tracking and 3D reconstruction.

7.3 OVINES trajectory extraction

7.3.1 Circle defined by 3 points in space

The coordinates of the Host wall are necessary in order to subsequently project the velocity of the NES in the normal and tangential directions to the wall at the time of impacts. To do this, 4 markers were placed on the contour of the wall. Only 3 points are needed to define a circle; thus, with 4 markers, 4 different circles can be drawn and the positions of their center and radius will be compared in order to assess the accuracy of the positioning of the 4 markers. Finally, the definitive wall considered for the future analyses will be the average of the positions of the 4 centers, and the average of the radii.

In space, the formulas for the center and radius of a circle defined by 3 points are the following:

$$\mathbf{a} = A - C, \tag{110}$$

$$\mathbf{b} = B - C, \tag{111}$$

$$P_0 = \frac{(\|\mathbf{a}\|^2\mathbf{b} - \|\mathbf{b}\|^2\mathbf{a}) \times (\mathbf{a} \times \mathbf{b})}{2\,\|\mathbf{a} \times \mathbf{b}\|^2} + \mathbf{C}, \tag{112}$$

$$r = \frac{\|\mathbf{a}\|\,\|\mathbf{b}\|\,\|\mathbf{a} - \mathbf{b}\|}{2\,\|\mathbf{a} \times \mathbf{b}\|}. \tag{113}$$

7.3.2 Rotation of the NES

The rotation of the NES can be deduced from the coordinates of 3 markers rigidly attached to the NES in the following way. Notably, by knowing the coordinates of these points, one can project one of the points onto the line linking the two others (Fig. 40).

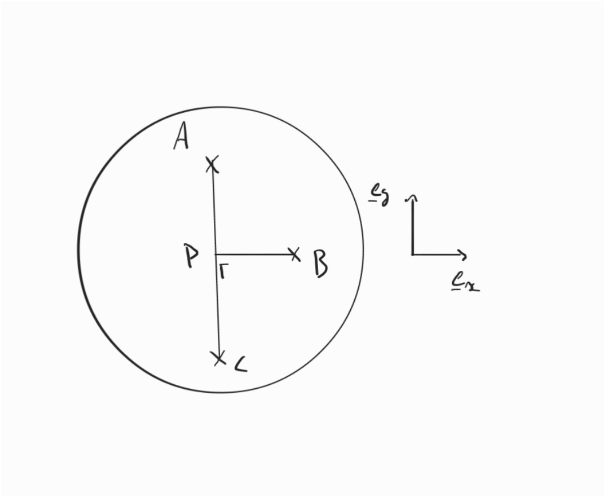

Figure 40: Geometrical method used to estimate the NES rotation from three tracked markers.

By doing so, it is possible to represent an orientation of the marker by:

$$cos(\theta) = \frac{\vec{PB}.\mathbf{e_x}}{\|\vec{PB}\|} \tag{114}$$

with

$$\vec{PB} = \vec{BC}.\vec{AC}\,\frac{\vec{AC}}{\|\vec{AC}\|} \tag{115}$$

by differentiating this orientation with respect to time, it is possible to know the rotational velocity of the NES.

7.3.3 Impact detection

The impact instants are identified using the following method.

Impacts correspond to sudden changes in velocity, which result in peaks in the acceleration signal. First, the coordinates of the NES center are smoothed using a Savitzky–Golay filter in order to reduce the effect of measurement noise. The velocities and accelerations are then obtained by numerical differentiation.

The acceleration norm is then computed, and the impact instants are identified as peaks of this acceleration norm. A minimum distance between two peaks and a prominence criterion are imposed in order to avoid detecting several peaks corresponding to the same impact.

7.4 Parameter identification method

The objective of this method is to identify the impact parameters of the model, namely the normal restitution coefficient ε, the friction coefficient μ_c and the tangential restitution coefficient β_0.

The impact model allows the post-impact velocity to be computed from the pre-impact velocity, the position at contact and the impact parameters. Therefore, if the experimental pre- and post-impact velocities are known, the model parameters can be estimated by comparing the experimental post-impact velocity with the velocity predicted by the model.

For each detected impact, the pre- and post-impact velocities are estimated from the reconstructed coordinates of the NES center and of the Host center. A local linear regression is performed on a few points before and after the impact. The points located too close to the impact are ignored, since the tracking can be less reliable at the impact instant. The slopes of the fitted straight lines then provide the velocities before and after impact.

Since the Host is also moving during the experiments, relative velocities are considered:

$$\dot{\mathbf{U}}_{\mathrm{rel}}^{-} = \dot{\mathbf{U}}_{N}^{-} - \dot{\mathbf{U}}_{H}^{-}, \tag{116}$$

$$\dot{\mathbf{U}}_{\mathrm{rel}}^{+} = \dot{\mathbf{U}}_{N}^{+} - \dot{\mathbf{U}}_{H}^{+}. \tag{117}$$

The local normal direction at the impact point is defined from the position of the NES center relative to the Host center:

$$\mathbf{e}_r = \frac{\mathbf{r}_N - \mathbf{r}_H}{\|\mathbf{r}_N - \mathbf{r}_H\|}. \tag{118}$$

The tangential direction is then defined as

$$\mathbf{e}_\theta = \begin{bmatrix} -e_{r,y} \\ e_{r,x} \end{bmatrix}. \tag{119}$$

The relative velocities are projected onto this local basis:

$$v_n^{-} = \dot{\mathbf{U}}_{\mathrm{rel}}^{-} \cdot \mathbf{e}_r, \qquad v_\theta^{-} = \dot{\mathbf{U}}_{\mathrm{rel}}^{-} \cdot \mathbf{e}_\theta, \tag{120}$$

$$v_n^{+} = \dot{\mathbf{U}}_{\mathrm{rel}}^{+} \cdot \mathbf{e}_r, \qquad v_\theta^{+} = \dot{\mathbf{U}}_{\mathrm{rel}}^{+} \cdot \mathbf{e}_\theta. \tag{121}$$

First, the normal restitution coefficient ε is identified by minimizing the relative error between the experimental and modelled normal post-impact velocities:

$$J_n(\varepsilon) = \left| \frac{v_{n,\mathrm{model}}^{+} - v_{n,\mathrm{exp}}^{+}}{v_{n,\mathrm{exp}}^{+}} \right|. \tag{122}$$

Then, the parameters μ_c and β_0 are identified from the tangential component of the velocity. A range of values of μ_c and β_0 is tested, and the post-impact tangential velocity predicted by the model is compared with the experimental one. The retained values are those minimizing the relative error:

$$J_t(\mu_c, \beta_0) = \left| \frac{v_{\theta,\mathrm{model}}^{+} - v_{\theta,\mathrm{exp}}^{+}}{v_{\theta,\mathrm{exp}}^{+}} \right|. \tag{123}$$

8 Experimental setup and measurement system

This section describes the experimental measurement system used during the tests. The setup includes the cameras, lighting system, synchronization devices, acquisition card and shaker configuration.

8.1 General setup

In order to carry out the experimental tests, a projector for lighting as well as two cameras (Fig. 41) will be used in order to observe the trajectory of the NES. More precisely, markers placed on the NES will make it possible to observe its trajectory and its rotation, as will be explained later.

To carry out the experimental tests, the following setup was implemented.

First of all, two cameras (shown in Fig. 41a) and 41b, which will make it possible to capture the trajectory and rotation of the Host, are used. The choice of two cameras rather than one is more suitable here, because they will allow a better precision in the acquisition of the data, given that acquisition with two cameras makes it possible to correct optical distortion problems. These are placed on tripods so that they are more stable.

A projector is also used, and placed as perpendicular as possible to the setup.

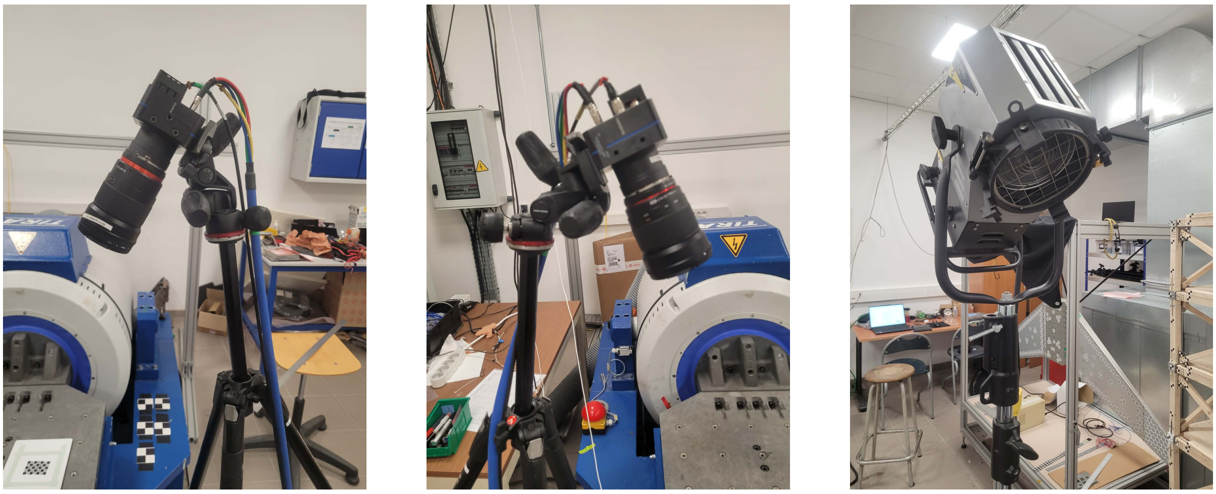

(a) Camera 1 (b) Camera 2 (c) Projector

Figure 41: Cameras and lighting system used for the experimental measurements.

The two cameras are each connected to a dedicated computer. These computers, using internal software, make it possible to adjust different acquisition parameters, such as the spatial resolution, the temporal resolution and the synchronization of the cameras. The cameras are also connected to a camera signal acquisition box (Fig. 42a). This box allows the cameras to be synchronized through a third trigger cable. This trigger cable is connected to an acquisition card (Fig. 42b).

The acquisition card makes it possible to observe the trigger signal. Indeed, this card is connected to one of the two computers and, through a software dedicated to triggering, it allows the synchronization parameters of the two cameras to be adjusted, such as the number of FPS and the camera exposure time. The acquisition card will also make it possible to observe the data from accelerometers that will be placed on future experimental setups.

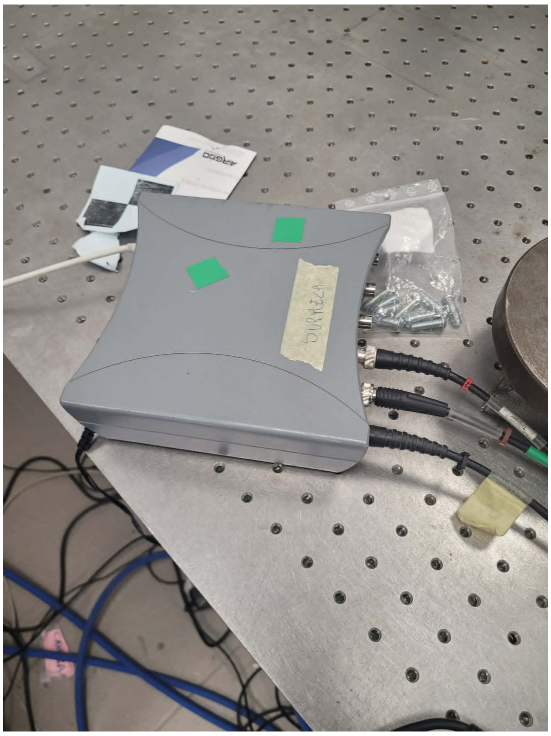

(a) Camera signal acquisition box

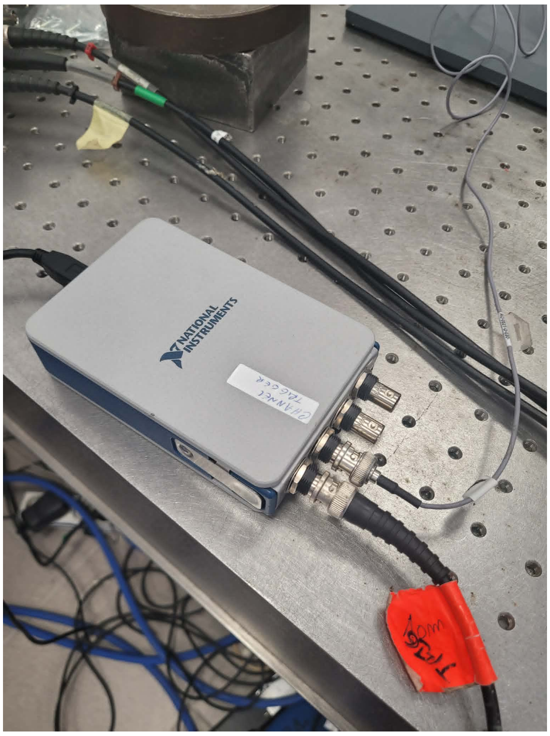

(b) Acquisition card

Figure 42: Camera synchronization and acquisition devices.

8.2 Configuration of the cameras

Internal software installed on the computers makes it possible to control the two cameras. In this software, it is first possible to adjust the spatial resolution of the cameras. The camera resolution is 12 megapixels (4096 x 3072 px) at 180 FPS. However, it is possible to adjust the spatial resolution in order to increase the number of FPS. For Vieworks cameras, the number of FPS can be increased by reducing the height in the resolution parameters. As indicated in the Vieworks user manual [21], the width does not influence the frame rate. Thus, to increase the frame rate by a factor of two, the vertical resolution should approximately be reduced by a factor of two [21]. Given the size of the Host wall, the vertical window was reduced as much as possible to 688 px, allowing an acquisition at 800 FPS .

When the spatial resolution is reduced, the image must also be centered in the parameters. Since the origin of the axes is located at the top left, the following formula must be applied:

```
H: Full-resolution height
D: Reduced height
```

Offset y: $\dfrac{H - D}{2}$

The software also makes it possible to launch a synchronized acquisition between the two cameras, by setting the following triggering parameters: the camera triggering period, corresponding to the inverse of the frame rate; the camera opening time (CamOn/CamOff) as well as the waiting time (Wait) before this opening.

8.3 Trigger signal and camera synchronization

The number of FPS was chosen to be 800; however, in practice, this number may change slightly between acquisitions. Fig. 43 shows a graph representing the experimental trigger signal (example of a signal from the 2nd series of experiments) superimposed on the theoretical signal with the following parameters. It can be observed that the period corresponding to 800 FPS is generally respected, but that variations may occur from one period to another.

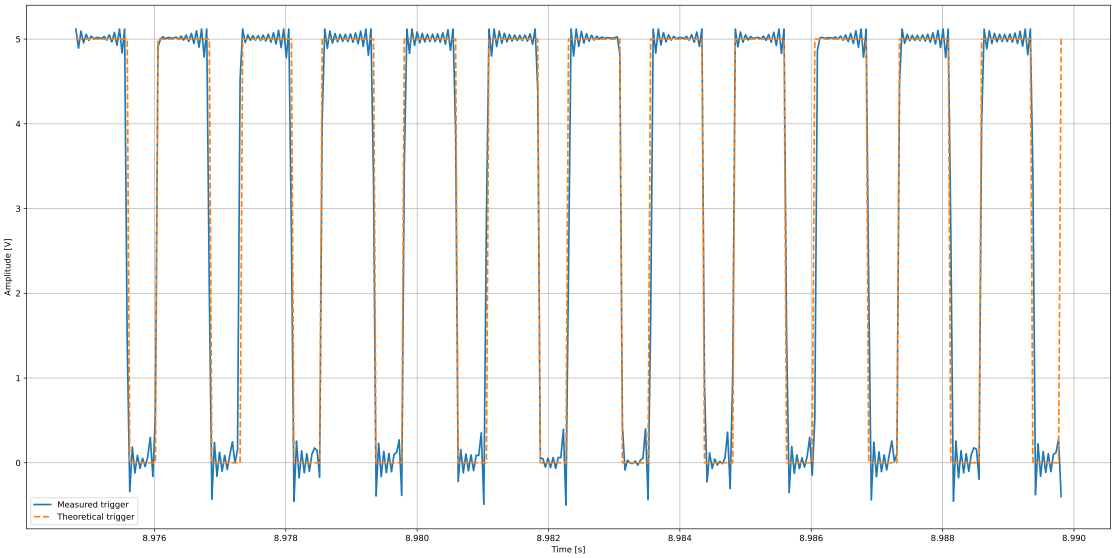

Figure 43: Comparison between the measured trigger signal and the theoretical trigger signal corresponding to an acquisition frequency of 800 fps.

8.4 OVINES configurations

Three experimental OVINES configurations were tested progressively. Each configuration was designed either to validate the measurement procedure or to reduce the limitations observed in the previous version.

8.4.1 Configuration : OVINES1

Objectives

For this first prototype, the objectives of the experimental tests will be purely qualitative. The Host will simply be fixed (without using the shaker) and the NES will be manually given initial impulses. The aim of this prototype will simply be to become familiar with the cameras and the post-processing software, to evaluate whether the NES markers can be properly tracked when it follows a rectilinear trajectory, when it is rotating and when it undergoes impacts with the Host. Different types of NES will also be tested in order to see which one is the most suitable for data post-processing. The prototype studied is the following.

Geometry, dimensions and prototype photographs

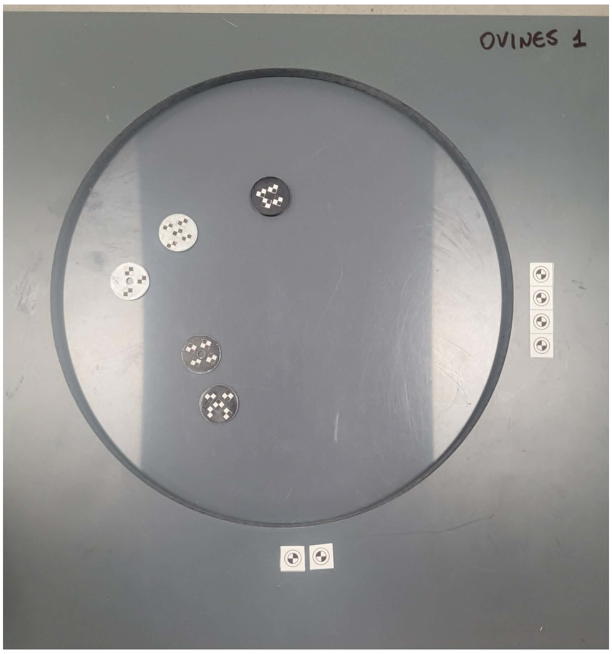

Figure 44: First OVINES experimental configuration used for preliminary qualitative tests.

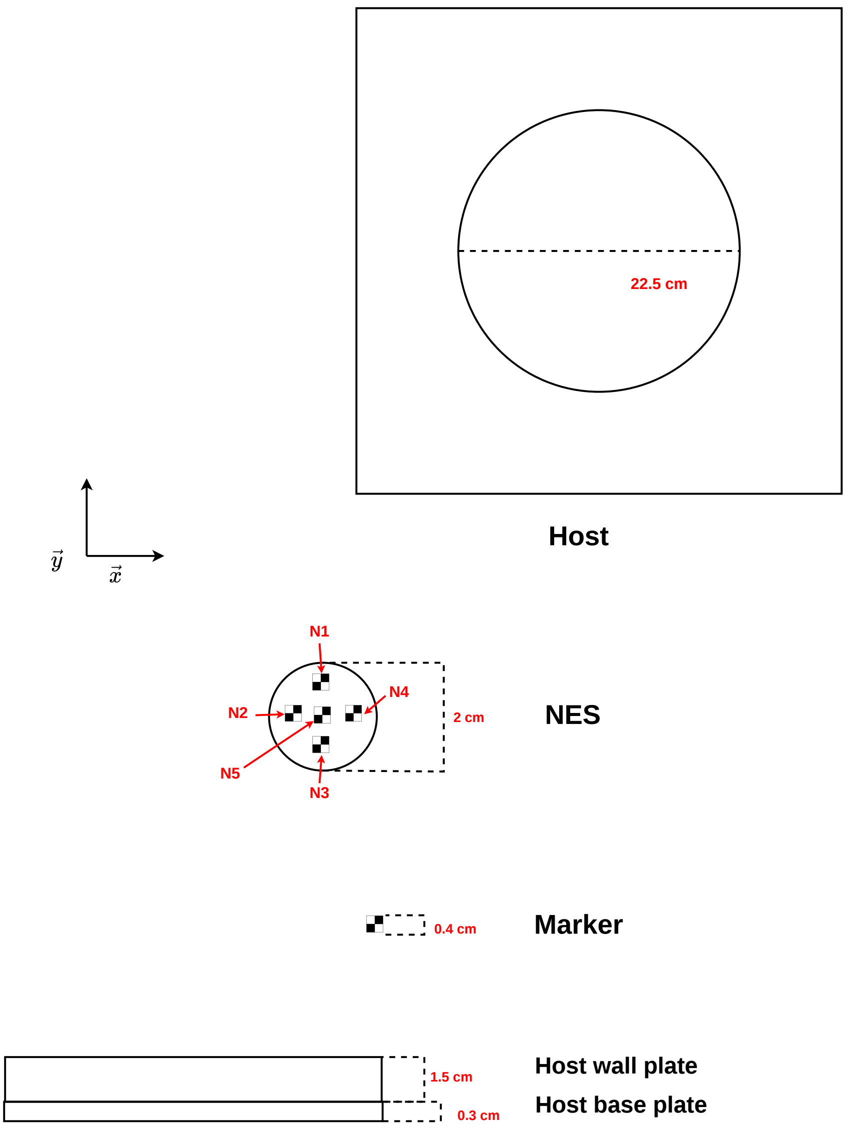

Figure 45: OVINES1 configuration: geometry, dimensions and marker numbering.

Materials

- Host plates: PVC
- NES: Washer made of steel

8.4.2 Configuration : OVINES2

Objectives

For this second prototype, a new Host was manufactured in order to be mounted on the shaker. The objective is to replace the manually imposed impulses used in the first prototype by a controlled harmonic excitation, allowing longer NES trajectories with more impacts to be observed.

The dimensions of the Host and of the NES are then chosen according to the shaker limitations and the reference amplitude proposed by [3].

Excitation of the shaker

According to the specifications, the following acceleration and frequency of the shaker will be considered:

$$\begin{aligned} a_{\text{pot\_vibrant}} &= 9g, \\ f &= 11 \text{ Hz}. \end{aligned}$$

The amplitude of the shaker can then be deduced:

$$\text{Amp} = \frac{a_{\text{pot\_vibrant}} \times 9.81}{(2\pi f)^2} \approx 1.848 \text{ cm}. \tag{124}$$

Knowing that the shaker must not move with an amplitude greater than 1 inch (= 2.54 cm), the amplitude is therefore sufficiently conservative.

Then, the study will be placed close to the amplitude of Sack [3], in order to deduce the radii of the Host and the NES, knowing that the radius of the NES is chosen to be 5 times smaller than that of the Host.

$$\text{Amp} = \frac{0.8L_g}{\pi} = \frac{2(R_H - R_N)}{\pi} = \frac{2R_H(1-0.2)}{\pi}. \tag{125}$$

By equating Eqs. 124 and 125, the following is obtained:

$$\frac{2R_H(1-0.2)}{\pi} = \frac{a_{\text{pot\_vibrant}} \times 9.81}{(2\pi f)^2}, \tag{126}$$

$$R_H = 4.536 \text{ cm}. \tag{127}$$

Since the study is still in the testing phase, a radius of 5 cm for the Host as well as a radius of 1 cm for the NES will therefore be considered for the sake of simplicity, and will then be adjusted better if necessary. Simulations of the numerical model with these values also give interesting results.

Geometry, dimensions and prototype photographs

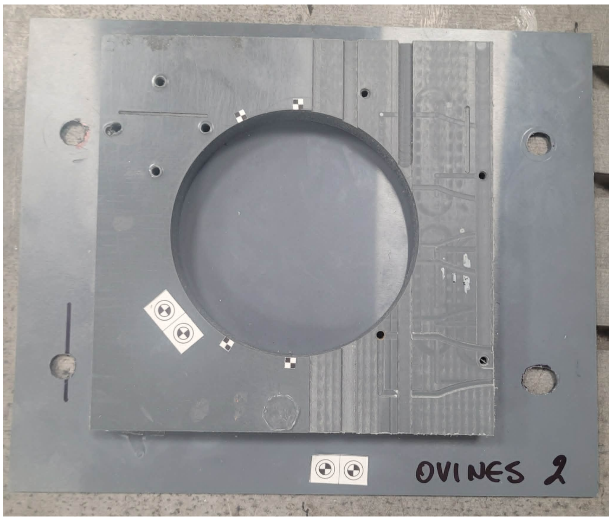

Figure 46: Second OVINES experimental configuration mounted on the shaker.

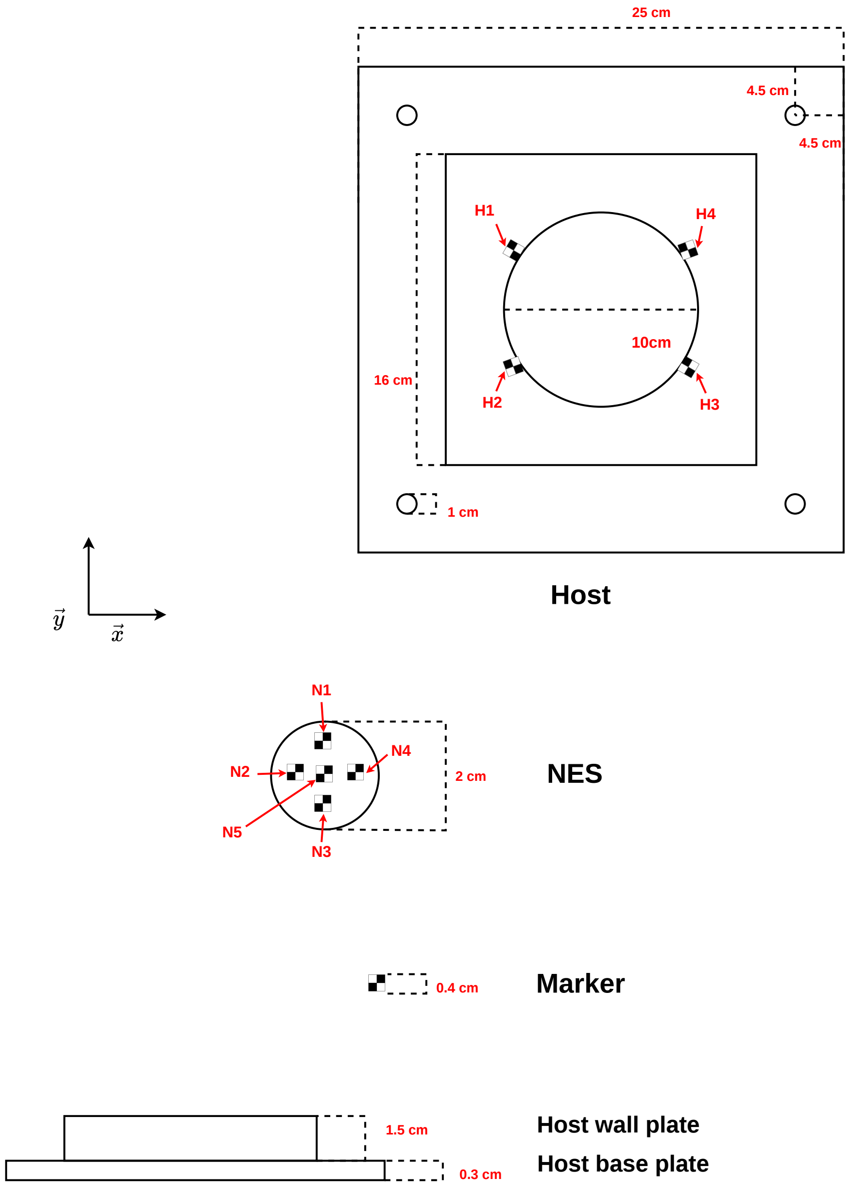

Figure 47: OVINES2 configuration: geometry, dimensions and marker numbering.

Materials

- Host plates: PVC
- NES: Washer made of steel

Experimental setup

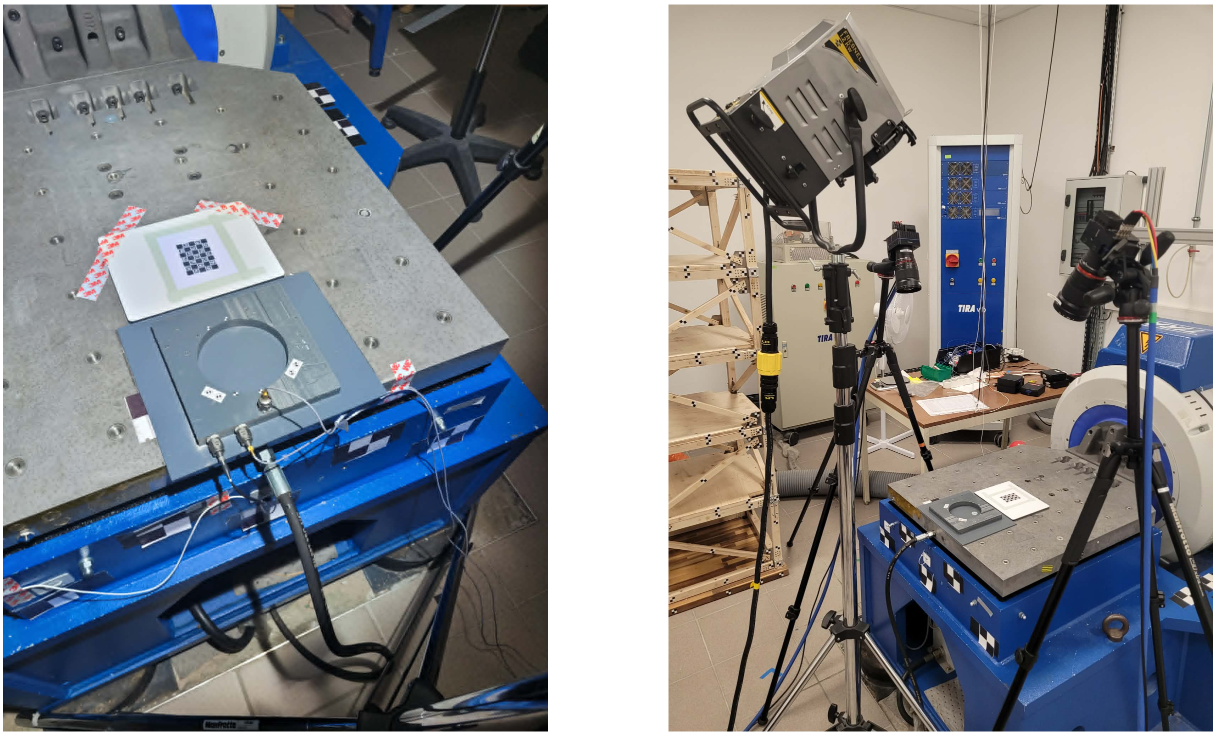

(a) Host mounted on the shaker　　(b) Shaker and support structure

Figure 48: Experimental setup of the OVINES2 configuration mounted on the shaker.

8.4.3 Configuration : OVINES3

In order to attempt to solve some of the problems and limitations of prototype 2, a third prototype was manufactured for which the following improvements were added:

- Markers were added on the shaker in order to know exactly the motion of the shaker. During the experiments with prototype 2, only markers were placed on the Host. Thus, it was not directly the motion of the shaker that was captured but the one transmitted to the Host by the shaker.
- A new visually cleaner plate was manufactured.
- The Host was screwed and glued with double-sided tape to the shaker.
- The washer representing the NES was sanded, and the wall of the Host was also sanded better than for the 2nd prototype.
- The thickness of the Host wall was chosen to be 1 cm instead of 1.5 cm in order to reduce shadowing problems and obstruction of the cameras' field of view.
- The markers present on the NES were brought closer to the center in order to reduce shadowing problems and obstruction of the cameras' field of view.
- New tripods were used, making it possible to bring the cameras closer to the direction perpendicular to the setup, thus reducing field of view obstruction problems. It is observed during post-processing that with this placement, this problem disappears completely.

Geometry, dimensions and prototype photographs

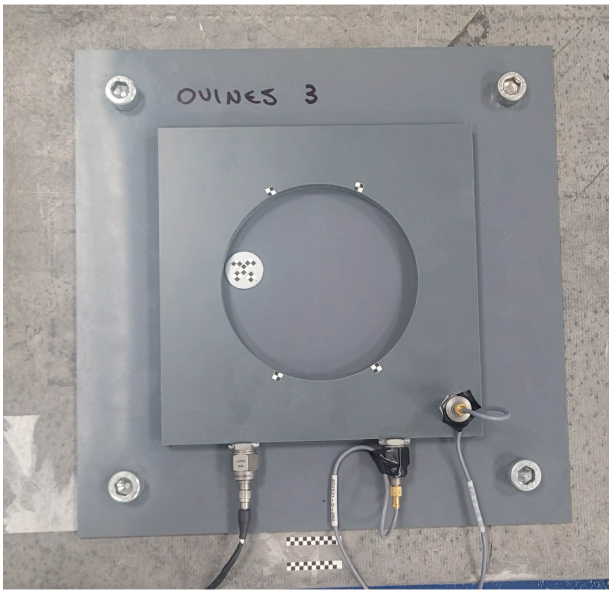

Figure 49: Third OVINES experimental configuration.

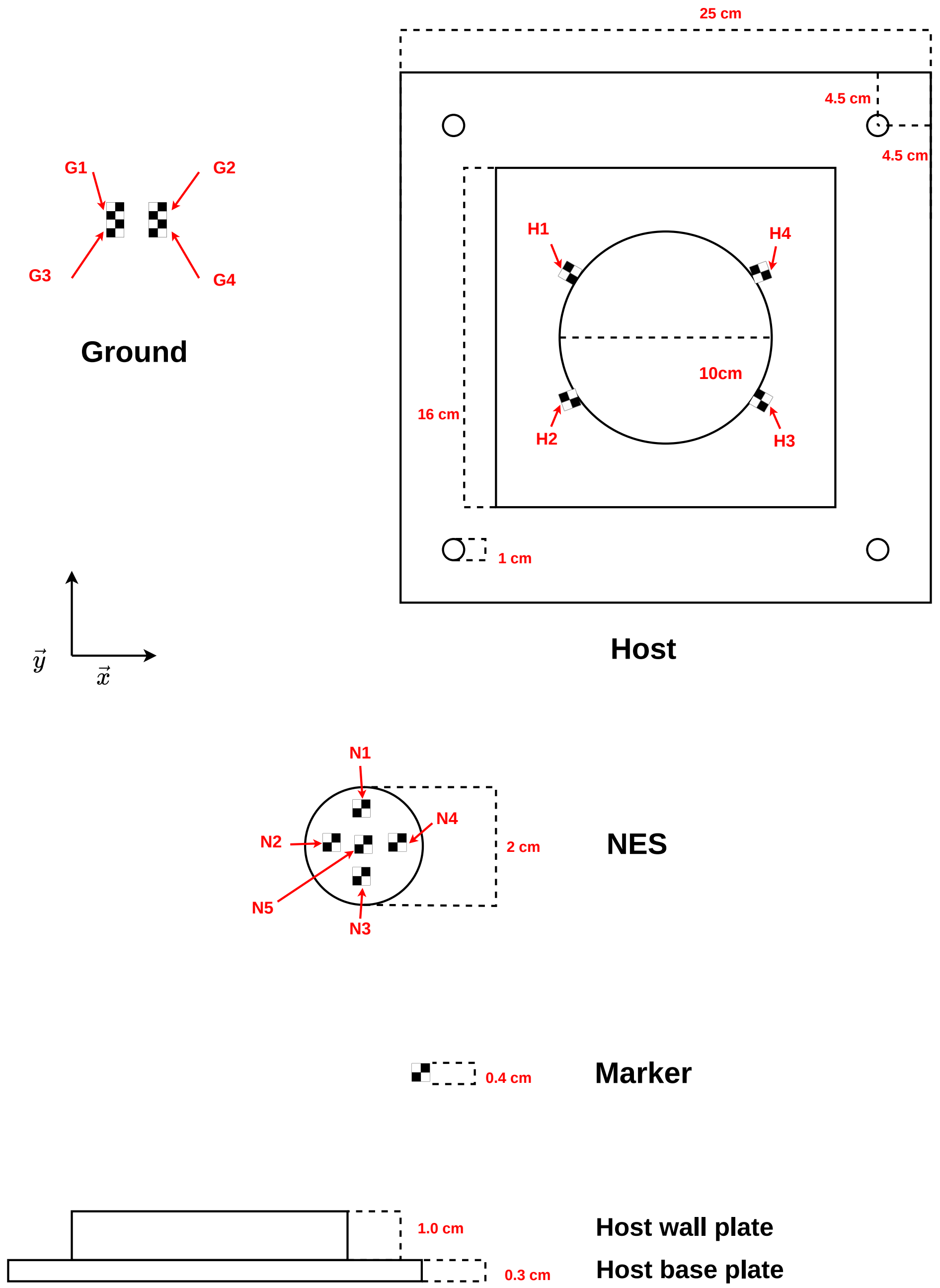

Figure 50: OVINES3 configuration: geometry, dimensions and marker numbering.

Materials

- Host plates: PVC
- NES: Washer made of steel

Experimental setup

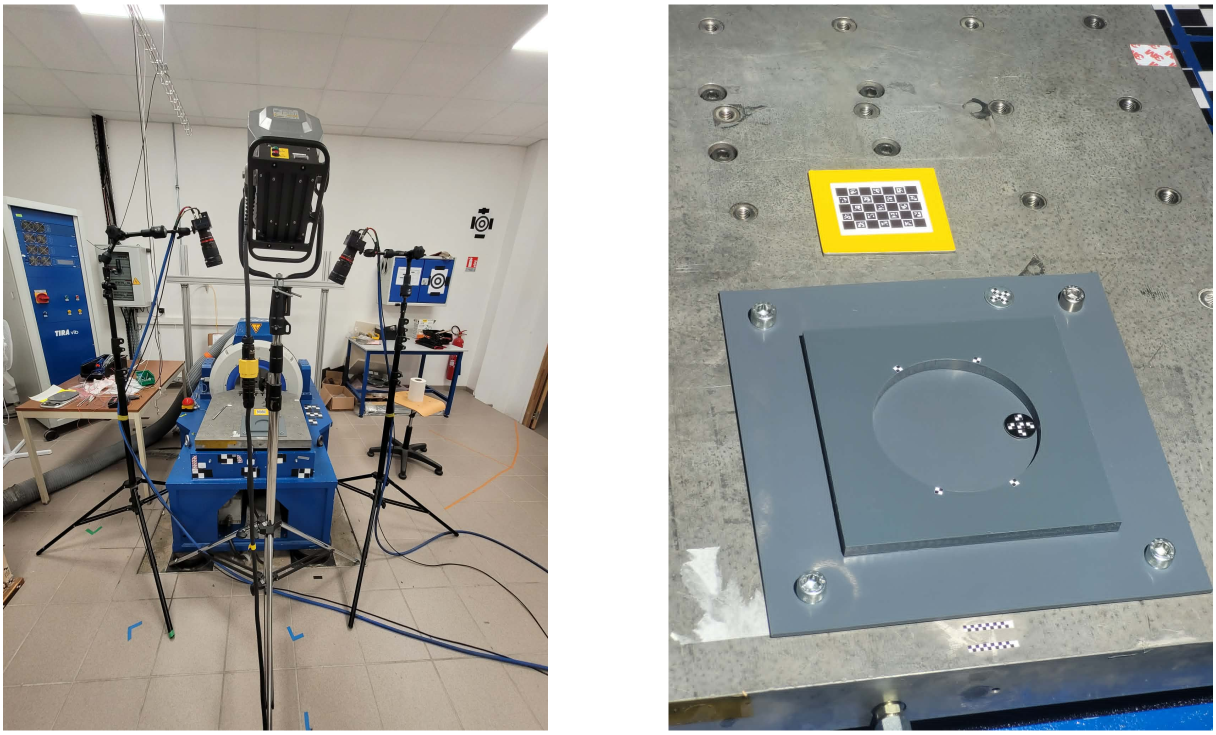

(a) First view of the OVINES3 experimental setup.

(b) Second view of the OVINES3 experimental setup.

Figure 51: Experimental setup of the OVINES3 configuration.

9 Results

This section presents the main experimental results obtained with the different OVINES configurations. The analysis focuses on the reconstructed marker motion, the NES trajectory, its rotation, the Host motion and the first identification of the impact parameters.

9.1 Assessment of an Ideal NES

In Fig. 52, different NESs used during the experiments can be seen. Respectively from top to bottom, the first one is a PVC cylinder of 2 cm diameter and 3 mm thickness painted in black. However, after several more or less identical launches, it was observed that the sliding of the NES decreased progressively. This behavior may be due to electrostatic interactions between the PVC NES and the Host, which could modify the friction conditions during the experiments. In any case, these NESs were not retained for the subsequent experiments. Then, a steel washer of 2 cm diameter and 1 cm thickness painted in white, then in black, then without paint can be seen. Two of these washers were painted in order to evaluate whether one of them would be more suitable for image processing.

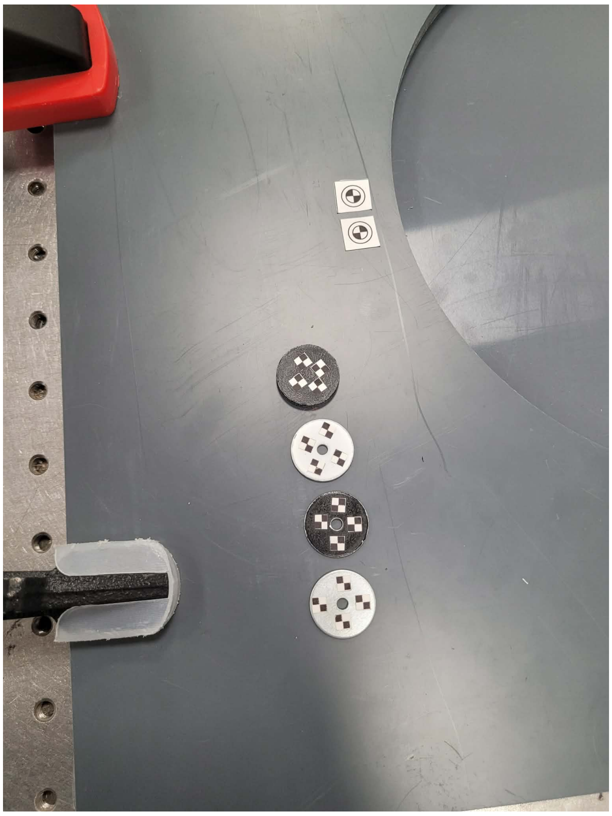

Figure 52: Photograph of the different internal masses used as NES during the experiments.

9.2 Results obtained with the OVINES2 configuration

The following results were obtained with the second OVINES configuration, using Test 1 from the OVINES2 experimental test series summarized in Table 18.

9.2.1 Markers motion

In order to better understand the data that will be discussed, the numbering of the markers used for the data processing is given in Fig. 53.

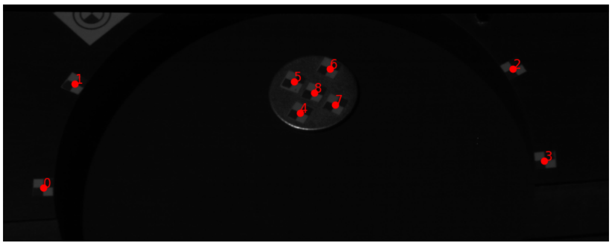

Figure 53: Markers label used for post-processing

After selecting the images folder, performing the camera calibration, selecting the markers and carrying out the tracking by each camera, the software VibrationTracker returns the coordinates of the different markers, which are displayed in Fig. 54.

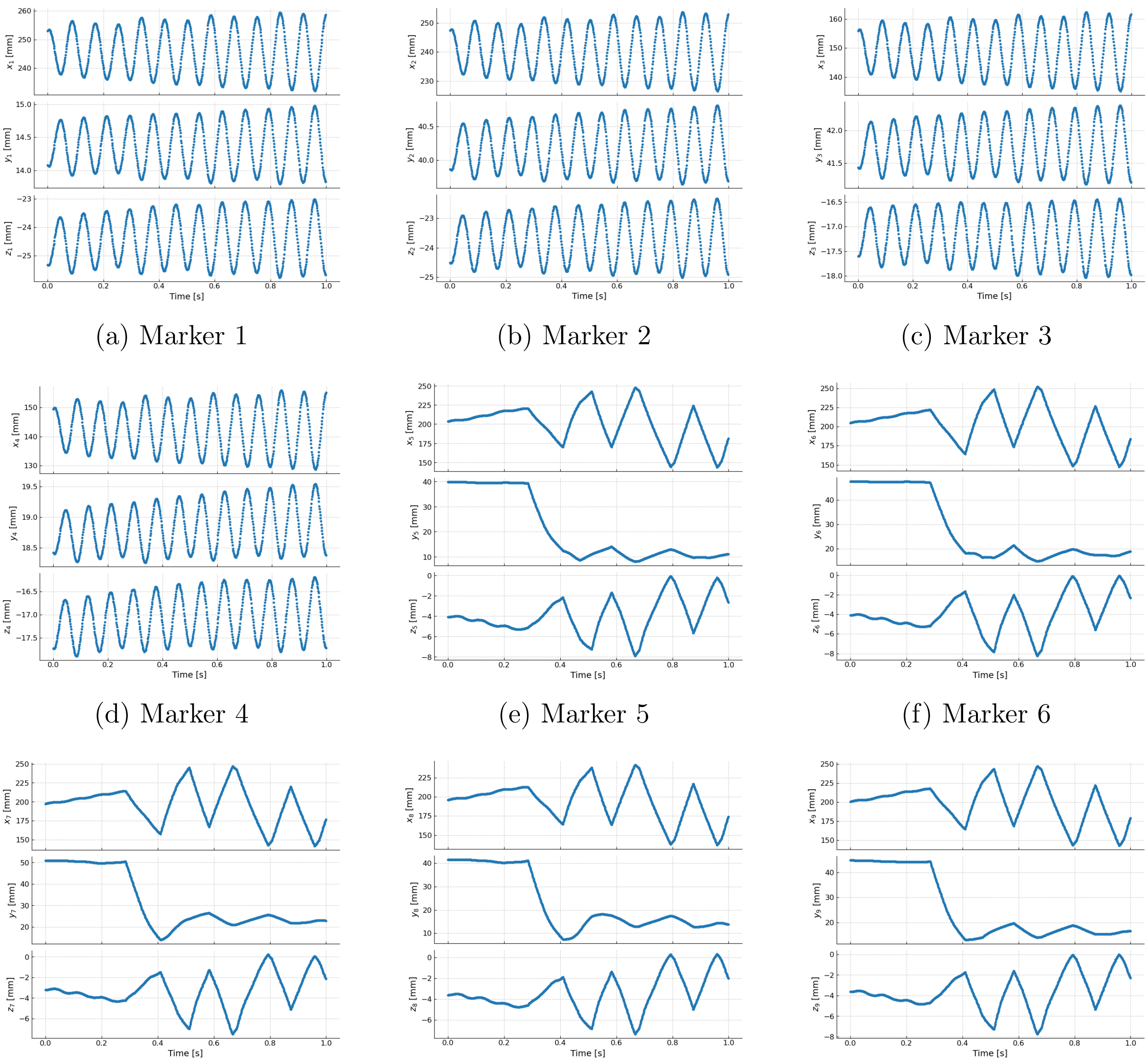

(a) Marker 1 (b) Marker 2 (c) Marker 3

(d) Marker 4 (e) Marker 5 (f) Marker 6

(g) Marker 7 (h) Marker 8 (i) Marker 9

Figure 54: Reconstructed marker coordinates along x, y and z over time.

The following observation can be made: the first 4 markers fixed to the Host are only supposed to move in the excitation direction; however, a small sinusoidal motion is also observed in the two other directions.

Distances between markers

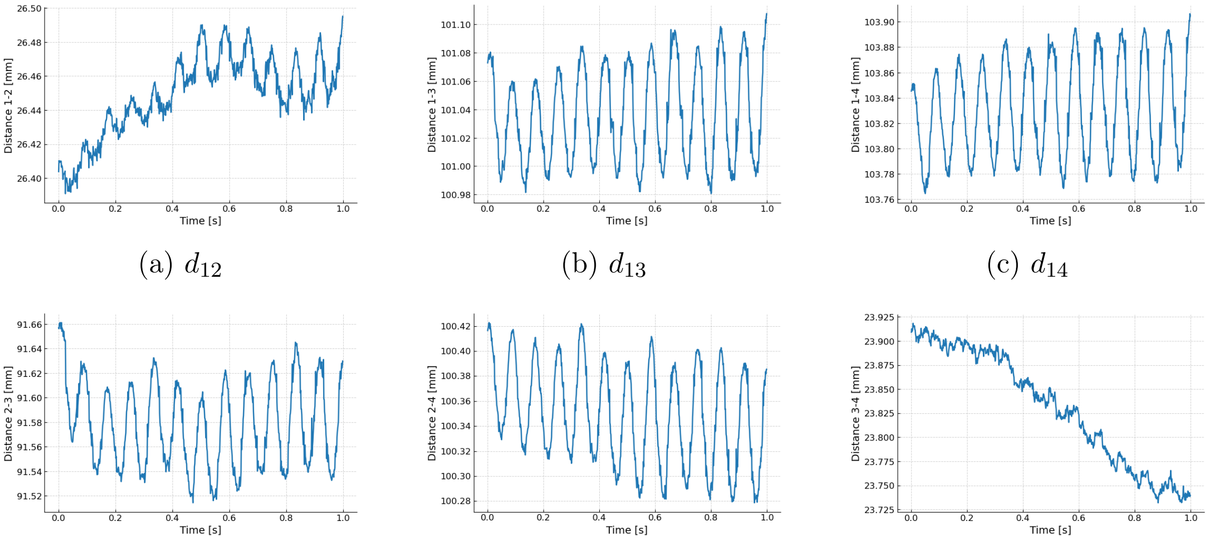

(a) d_{12} (b) d_{13} (c) d_{14}

(d) d_{23} (e) d_{24} (f) d_{34}

Figure 55: Distances between the Host markers over time.

Figure 55 shows the distances between the four markers placed on the Host over time, which is expected to be constant for a rigid Host. Variations due to camera noise of the order of 0.1 mm can be observed.

Distances between the centers of the circles

In Fig. 56, the distances over time between the different centers of the circles arising from the 4 markers and evaluated according to Sec. 7.3.1 are represented. An maximum error of 0.35 mm is observed.

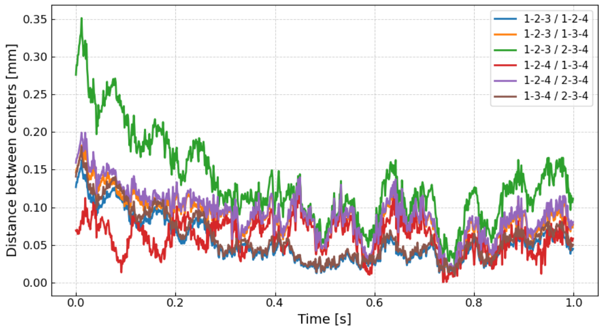

Figure 56: Distances between the centers of the circles evaluated from 4 markers.

9.2.2 Experimental trajectory of the OVINES

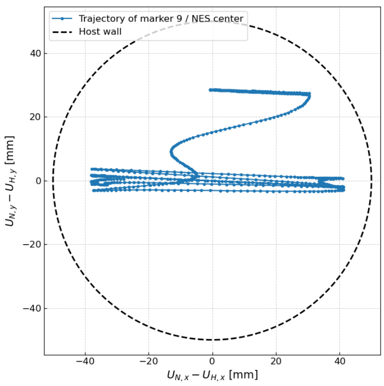

(a) Relative trajectory of the NES with respect to the Host

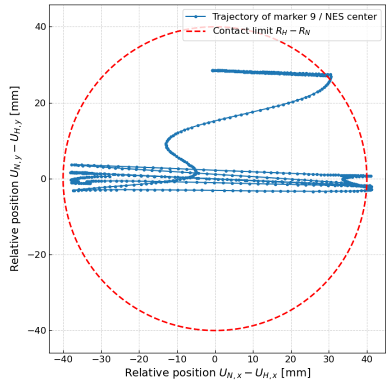

(b) Relative trajectory of the NES with respect to the Host, considering a contact radius for the Host

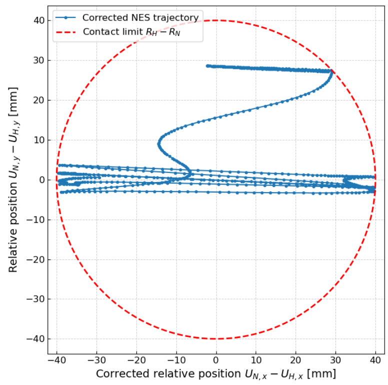

(c) Relative trajectory of the NES with respect to the Host, considering a contact radius for the Host, with the addition of an offset along x

Figure 57: Relative trajectory of the NES for the OVINES2 configuration.

Figure 57 shows the relative trajectory of the NES with respect to the Host. First, the trajectory is represented inside the reconstructed Host wall. Then, the NES radius is subtracted from the Host radius in order to represent the theoretical contact edge. Finally, an offset along the x direction is applied to correct the relative positioning of the trajectory.

Rotation of the NES

By using markers 5-6-7-8, it is possible to represent $C_4^3 = 4$ combinations of 3 markers in order to know the rotational velocity of the NES over time according to Sec.7.3.2. By doing so, the graph of Fig. 58b is obtained.

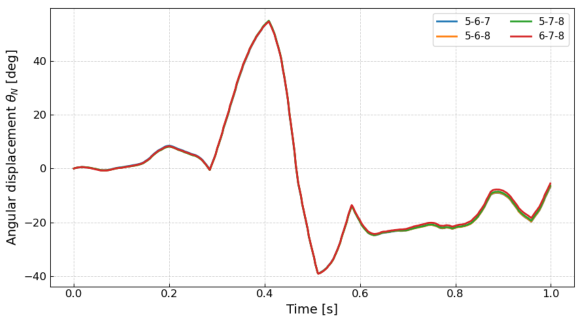

(a) Angular evolution of the NES according to its possible marker combination

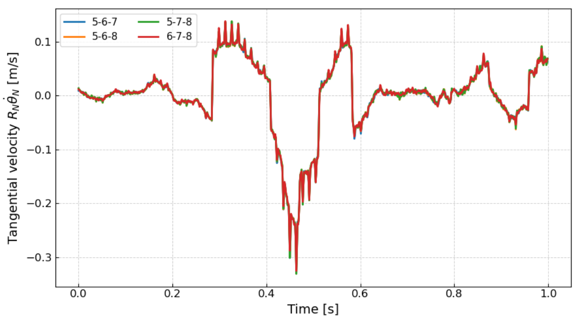

(b) Rotational velocity of the NES according to its possible marker combinations

Figure 58: Angular position and rotational velocity of the NES reconstructed from different marker triplets.

It is then observed on this graph that the rotational velocities obtained from different combinations are very close. It is then possible to calculate the derivative of these rotational velocities at each instant in order to define the experimental rotational velocity of the NES (Fig. 58b).

Translational velocities of the NES and the Host

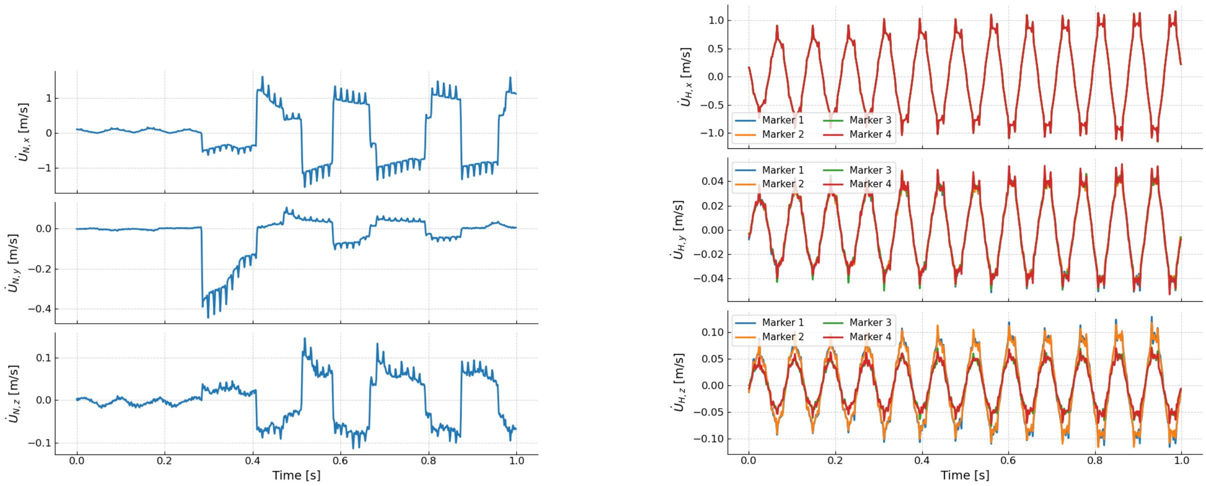

(a) Velocities of the NES along x, y and z in the absolute frame

(b) Velocities of the four Host markers along x, y and z in the absolute frame

Figure 59: Translational velocities of the NES and Host markers for the OVINES2 configuration.

The velocities shown in Fig. 59 were obtained by differentiating the reconstructed marker positions with respect to time. The figure shows the velocity components of the NES and of the Host markers in the absolute frame. Several peaks can be observed in the velocity signals, especially for the NES.

9.3 Results obtained with the OVINES3 configuration

The following results were obtained with the third OVINES configuration, using Test 5 from the OVINES3 experimental test series summarized in Table 20. This configuration was designed to reduce the main limitations observed with OVINES2. The results presented below focus on the reconstructed motion and on the first attempt to identify the impact parameters.

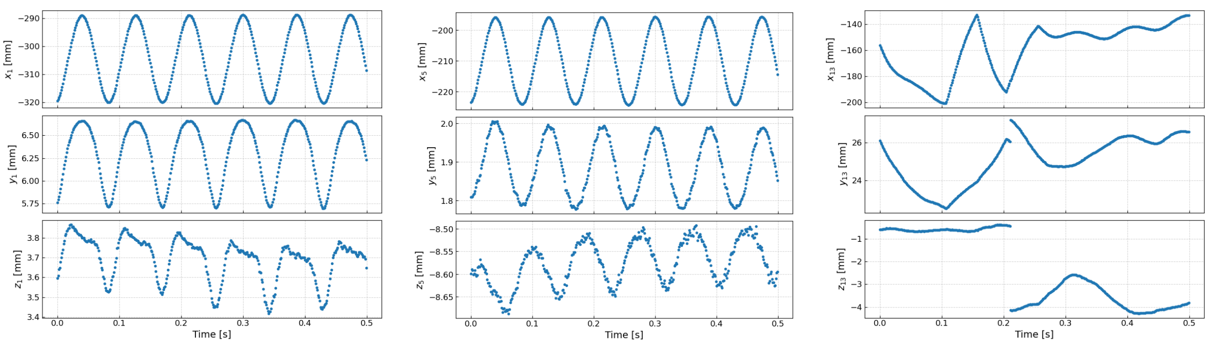

(a) Coordinates of marker G1 (b) Coordinates of marker H1 (c) Coordinates of marker N1

Figure 60: Representative reconstructed coordinates of markers G1, H1 and N1 for the OVINES3 configuration.

Figure 60 shows the reconstructed coordinates of three representative markers of the OVINES3 configuration: one marker fixed to the ground, one marker fixed to the Host and one marker fixed to the NES.

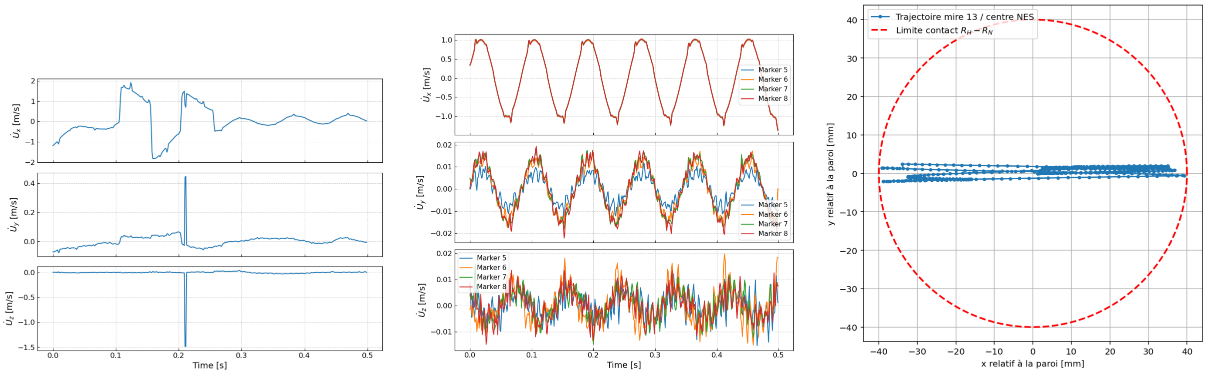

(a) NES translational velocity (b) Host translational velocity (c) Relative NES trajectory

Figure 61: NES and Host velocities and relative NES trajectory for the OVINES3 configuration.

Figure 61 shows the translational velocity of the NES, the translational velocity of the Host, and the relative trajectory of the NES with respect to the Host for the OVINES3 configuration.

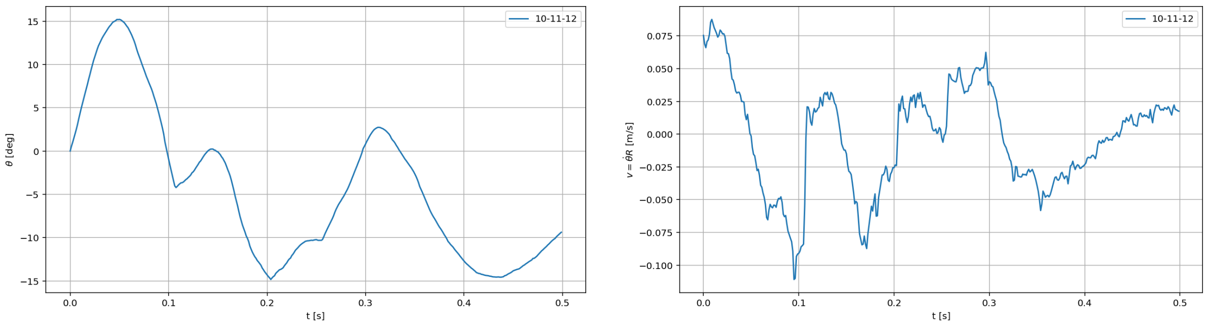

(a) NES angular position (b) NES rotational velocity

Figure 62: Angular position and rotational velocity of the NES for the OVINES3 configuration.

Figure 62 shows the angular position and rotational velocity of the NES for the OVINES3 configuration.

9.3.1 Parameter identification

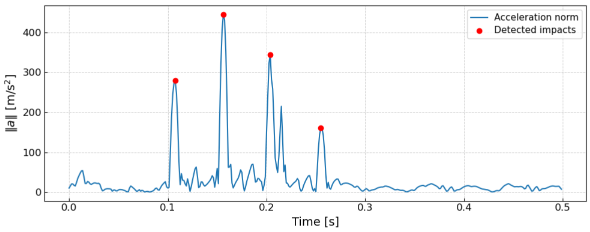

(a) Detected impacts on the acceleration norm

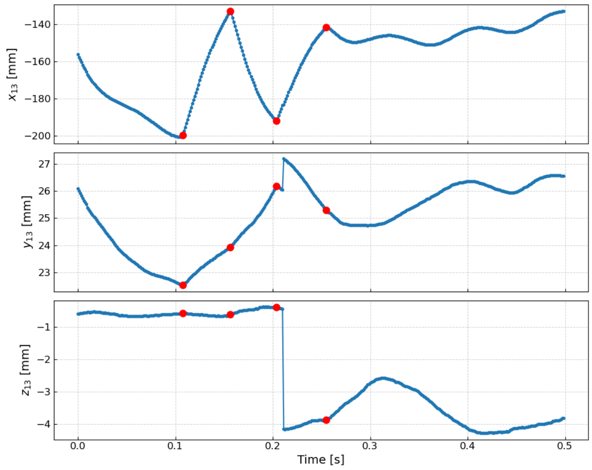

(b) Detected impacts on the NES center coordinates

Figure 63: Impact detection from the reconstructed acceleration norm and corresponding NES coordinates.

Figure 63 shows the impact instants detected from the peaks of the acceleration norm. It can be observed that these instants correspond to abrupt changes in the slope of the reconstructed NES center coordinates.

9.3.2 Normal restitution coefficient ε

Table 16: Normal restitution coefficient identified from five impacts

Impact number	ε
1	0.87
2	0.78
3	0.74
4	0.53
5	0.67
Mean	0.72
Standard deviation	0.12

Table 16 reports the values of the normal restitution coefficient ε identified from five selected impacts. The identified values range from 0.53 to 0.87, with a mean value of 0.72 and an observed standard deviation of 0.12.

9.3.3 Friction coefficient for collision μ_c and tangential restitution coefficient β_0

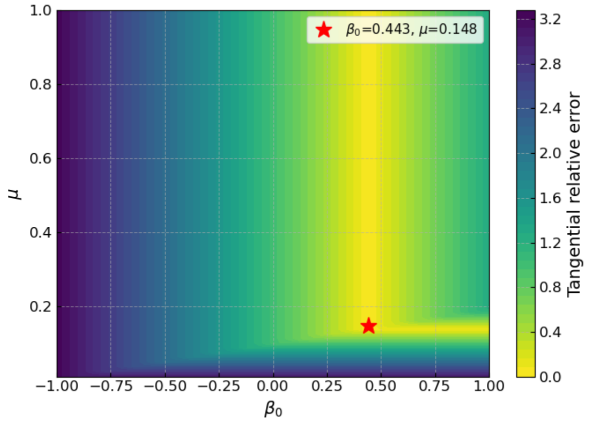

(a) Impact 1

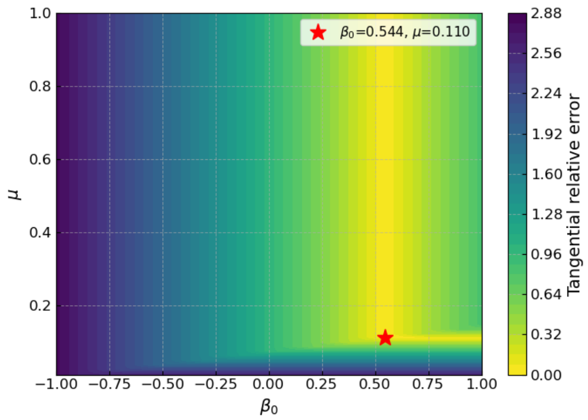

(b) Impact 2

Figure 64: Error maps for the identification of μ_c and β_0 from two selected impacts.

Figure 64 shows the error maps obtained for the identification of μ_c and β_0 from two selected impacts. For the first impact, the minimum error is obtained for $\beta_0 = 0.443$ and $\mu_c = 0.148$. For the second impact, the minimum error is obtained for $\beta_0 = 0.544$ and $\mu_c = 0.110$. The corresponding mean values are therefore approximately $\overline{\beta_0} = 0.494$ and $\overline{\mu}_c = 0.129$. The second impact corresponds to the first rebound of Test 6 from the OVINES3 experimental test series summarized in Table 20.

10 Discussion and limitations

This section discusses the main limitations observed during the experimental study.

10.1 Analysis of the experimental results

It can be observed in Fig. 58b that there are peaks in the graph. These are probably due to the numerical differentiation of experimental data. It can be observed that the graph of the evolution of the NES angle is, for its part, cleaner (Fig. 58a).

The parameter identification should be considered as preliminary, since only a limited number of impacts were analysed. A more reliable recalibration would require the analysis of a larger number of impacts, obtained from several experimental tests. This would allow mean values and standard deviations to be computed over a larger sample, and would provide a better estimate of the dispersion of the identified parameters. These results must also be put into perspective with the limitations presented below.

10.2 Limitations of OVINES1

The post-processing results of this first prototype made it possible to observe the following:

- The PVC NES was not retained because its friction appears to change significantly after a few tests.
- The tracking of the markers by the cameras appears to be similar whether the NES is painted, either white or black, or left unpainted.
- The manually applied impulses obstruct the cameras' fields of view, and the NES remains in motion for only a few seconds before stopping. Thus, the use of a shaker seems appropriate to analyze larger trajectories with more impacts, which will make it possible to perform a better parameter identification of the model.

10.3 Limitations of OVINES2

The experimental tests on this second prototype presented the following limitations:

- As can be seen in Fig. 54a, Fig. 54b, Fig. 54c and Fig. 54d, the Host undergoes relatively large displacements along z (of the order of 1–2 mm peak-to-peak). This adds a lot of imprecision to the results, given that planar motion is desired. Furthermore, during the analysis of the trajectories, the motion of the NES and of the Host is projected only along the $\vec{X}$ and $\vec{Y}$ axes, which may notably explain the offset observed in the reconstructed trajectory.
- The thickness of the Host wall plate is 1.5 cm. This large thickness generates several problems in the tracking of the NES markers.

  Indeed, first, this induces large shadowed areas during the experiments, and when the markers pass through these areas, the cameras lose their tracking.

Then, since the cameras are placed obliquely with respect to the setup, the edges of the wall also hide a distinct part of the setup from each camera. This therefore induces areas in the Host in which the tracking of the markers is lost when they pass through them.

Since these areas are located at the extremities of the Host in the direction perpendicular to the excitation, this therefore did not cause problems for all the experiments, and a fortiori for the analyzed one. However, the purpose of the experimental tests is to be able to track the NES in all areas of the Host, therefore it is essential to remedy this problem.

- Visually, the plate is shapeless and not very presentable.
- The Host is glued to the shaker only with double-sided tape. A better fixation method may have to be used.

10.4 Limitations of OVINES3

This third series of tests also showed a certain number of limitations. These limitations and problems are the following:

- As can be seen on the summary sheet of the tests carried out on prototype 3, the accelerations used are lower than in the previous tests; and with this new series of tests, it was observed that the impulse induced by the first rebound on the NES does not allow it to reach another edge of the wall and continue a bidirectional trajectory. Indeed, this first impulse only allowed the NES to move towards the center of the Host, thus subsequently causing a trajectory practically only in the direction of the excitation as can be seen in Fig. 61c. This kind of trajectory is problematic in the context of parameter identification because in order to perform a parameter identification on the parameters μ_c and β_0, this requires relatively high tangential velocities so that they prevail over the measurement noise. Therefore, only the first rebound of each test can be used to identify β_0 and μ_c.
- During the 3rd series of experiments, an attempt to improve the trigger parameters was carried out. Indeed, the following parameters were used:

$$CamOn = 300\mu s \tag{128}$$
$$CamOff = 600\mu s \tag{129}$$
$$Wait = 1250\mu s \tag{130}$$

instead of the following parameters used during the 2nd series of experiments:

$$CamOn = 100\mu s \tag{131}$$
$$CamOff = 900\mu s \tag{132}$$
$$Wait = 1250\mu s \tag{133}$$

The goal was to improve the detection of the markers by the cameras and to extend the tracking duration of the markers. However, this change instead had the opposite effect and reduced the quality of the detection of the markers by the cameras, thus inducing shorter marker tracking durations.

- Finally, bringing the markers closer to the center of the NES was not necessary. Indeed, the NES markers of the washer from the 2nd series of experiments were clearly visible by the cameras regardless of their position on the Host (thanks to the reduction in thickness of the Host plate); however, unfortunately, bringing the NES markers closer to one another caused tracking errors.

  This problem also contributed to the fact that the tracking during this 3rd series of experiments was possible over shorter durations than during the 2nd series of experiments.

10.5 Overall limitations

- More generally, the performances of the shaker with the configurations used during the experiments do not allow the first impulse given to the NES to directly reach the other edge of the Host.
- Currently, the determination of the Host wall and the center of the NES with markers is rather imprecise.
- It can be observed that the PVC of the Host (lower plate) becomes scratched throughout the experiments, thus modifying the friction between the NES and the ground.
- The number of fps of the cameras may be slightly too low to properly track the NES markers during the total trajectory of the NES. However, it should be verified whether it is possible to better track the markers through other adjustments than increasing the number of fps.
- The shaker heats up throughout the experiments (going from 21°C to 26°C during the tests of the 3rd series of experiments). It should therefore be investigated whether this temperature increase may affect the properties of the PVC.
- Washers were used to represent the NES, however these have a circular hole of 1 mm in diameter at their center.

10.6 Perspectives for improving the experiments

A list of limitations was presented previously. In this section, a series of improvements will be proposed for future experiments.

- Code a method allowing the reconstruction of the Host wall, as well as the NES wall, from their images on the two cameras. Successfully coding this would not only allow a better precision in the localization of the Host walls as well as the center of the NES, but it would also allow the removal of the marker placed at the center of the NES so that it would improve the tracking of the markers.

- Since the shaker heats up throughout the experiments, it should be investigated whether this temperature increase may affect the properties of the PVC. This problem was not directly observed, but it would be preferable to prevent it in future experiments, for example by considering a material for the Host with better thermal stability.

- Use thin cylinders instead of washers for the NES.

- It was mentioned that the experimental configurations did not allow the first impulse of the NES to directly reach another edge of the wall. So, in all tests, the NES moves near the center of the Host after the first impact and then its trajectory is essentially in the direction of the excitation. To remedy this problem, two possible solutions are proposed. First, the friction between the NES and the ground could be reduced either by using other materials, or by lubricating the NES and/or the ground with oil, talc. Another, more innovative and interesting solution would be to use the following model.

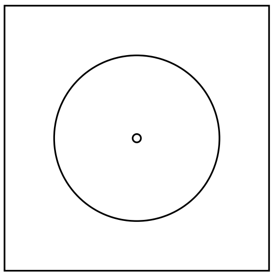

Figure 65: Proposed improved experimental configuration with a fixed central obstacle.

  This new setup consists in adding a fixed central cylinder at the center of the Host, making it possible to naturally induce chaos in the trajectory of the NES,

- Another possible perspective would be to modify the geometry of the experimental setup in order to promote a more bidirectional motion of the NES. In the present configuration, the motion remains mainly aligned with the excitation direction, which limits the amount of tangential information available at impact.

  For this purpose, the contact law should first be reconsidered in order to determine whether it can be adapted to impacts between a circular NES and a flat surface of the Host plate. If this approach is applicable, a triangular Host geometry could then be investigated. Such a geometry would force the NES to impact surfaces with different orientations and would therefore promote a more bidirectional trajectory.

Part III

Conclusion

The objective of this work was to study an omnidirectional vibro-impact nonlinear energy sink composed of an internal cylindrical mass moving inside a circular Host. The work was divided into two main parts: the development of numerical models and the experimental study of several OVINES configurations.

First, a numerical OVINES model was developed in Python. In this first model, the gravitational force was taken into account for the NES in order to perform different validation tests (energy conservation, comparison of rebound heights with theoretical values).

Then, friction was added to the model by using the model of Farkas [2]. The implementation of friction is consistent with the results of the article, and also satisfies the Rabinowicz test [1].

A new model was also studied. This new model consists in adding springs and dampers between the Host and the ground, while friction is not considered. This model shows that successive impacts transfer part of the energy from the Host to the NES and redistribute the motion among the translational and rotational degrees of freedom.

A final interesting case was analysed qualitatively. It can be observed that when energy dissipation by friction is added (in a model where the Host is subjected to a harmonic excitation), it counter-intuitively leads to larger NES velocity components in the x and θ directions, as well as to a larger number of rebounds.

The second part of the work focused on the experimental study. A two-camera measurement setup was used to reconstruct the three-dimensional motion of the system. Several OVINES configurations were tested. OVINES1 was used for preliminary qualitative tests and for becoming familiar with the cameras, the markers and the post-processing software. OVINES2 introduced a shaker excitation and allowed the relative trajectory of the NES with respect to the Host to be reconstructed. OVINES3 was then designed to reduce some limitations of OVINES2 by adding markers on the ground, improving the fixation of the Host, reducing the Host wall thickness and modifying the marker positions.

The post-processing method made it possible to estimate the Host centre and radius, reconstruct the relative trajectory of the NES, estimate the angular position and rotational velocity of the NES, and detect the main impact instants from the acceleration norm. These steps allowed the motion of the NES and Host to be analysed from the experimental measurements.

A first parameter identification was performed using selected impacts. The normal restitution coefficient was identified from five impacts, giving a mean value of approximately 0.72 and a standard deviation of 0.12. The collision friction coefficient μ_c and the tangential restitution coefficient β_0 were estimated from two selected impacts, giving indicative mean values of approximately $\overline{\mu}_c = 0.129$ and $\overline{\beta_0} = 0.494$.

These values should be considered as preliminary estimates, since only a limited number of impacts were analysed. Furthermore, these results must be considered while keeping in mind the different limitations and accuracy levels of the experimental tests, including uncertainties in the position of the NES centre, the Host walls, and inaccuracies due to marker tracking.

Overall, this work made it possible to build and validate a numerical framework for the OVINES dynamics, to develop an experimental measurement procedure, and to obtain a first reconstruction of the NES motion and a preliminary identification of the impact parameters.

Future work should focus on reducing the experimental limitations identified in this report. One of the main limitations is that, in the present tests, the NES trajectory remained mainly aligned with the excitation direction of the Host. This limited the motion of the NES in the transverse direction and in rotation.

Two alternative geometries could therefore be investigated in order to promote a more bidirectional motion of the NES. The first one would consist of adding a fixed central cylinder inside the Host. The second one would consist of using triangular Host walls. This second configuration would first require verifying whether the impact model can be adapted to describe the contact between a circular NES and a flat wall.

Use of artificial intelligence

Artificial intelligence tools were used during the writing of this report as support for translation, reformulation, LaTeX formatting, Python plots and coding assistance.

References

[1] Ettore Pennestrì, Valerio Rossi, Pietro Salvini, and Pier Paolo Valentini. Review and comparison of dry friction force models. *Nonlinear Dynamics*, 83(4):1785–1801, November 2015.

[2] Zénó Farkas, Guido Bartels, Tamás Unger, and Dietrich E. Wolf. Frictional coupling between sliding and spinning motion. *Physical Review Letters*, 90(24):248302, June 2003.

[3] Achim Sack, Michael Heckel, Jonathan E. Kollmer, Fabian Zimber, and Thorsten Pöschel. Energy dissipation in driven granular matter in the absence of gravity. *Physical Review Letters*, 111(1):018001, July 2013.

[4] Xiao-Feng Geng, Hu Ding, Jin-Chen Ji, Ke-Xiang Wei, Xing-Jian Jing, and Li-Qun Chen. A state-of-the-art review on the dynamic design of nonlinear energy sinks. *Engineering Structures*, 313:118228, August 2024.

[5] Mohammad A. AL-Shudeifat. Highly efficient nonlinear energy sink. *Nonlinear Dynamics*, 76(4):1905–1920, January 2014.

[6] Peng Zhou and Hui Li. Modeling and control performance of a negative stiffness damper for suppressing stay cable vibrations: Modeling and control performance of a negative stiffness damper. *Structural Control and Health Monitoring*, 23(4):764–782, October 2015.

[7] Yangyang Chen, Zhichao Qian, Kai Chen, Ping Tan, and Solomon Tesfamariam. Seismic performance of a nonlinear energy sink with negative stiffness and sliding friction. *Structural Control and Health Monitoring*, 26(11), August 2019.

[8] S. Lo Feudo, C. Touzé, J. Boisson, and G. Cumunel. Nonlinear magnetic vibration absorber for passive control of a multi–storey structure. *Journal of Sound and Vibration*, 438:33–53, January 2019.

[9] S. Benacchio, A. Malher, J. Boisson, and C. Touzé. Design of a magnetic vibration absorber with tunable stiffnesses. *Nonlinear Dynamics*, 85(2):893–911, March 2016.

[10] G. Pennisi, B.P. Mann, N. Naclerio, C. Stephan, and G. Michon. Design and experimental study of a nonlinear energy sink coupled to an electromagnetic energy harvester. *Journal of Sound and Vibration*, 437:340–357, December 2018.

[11] Mohammad A. AL-Shudeifat, Nicholas E. Wierschem, Lawrence A. Bergman, and Alexander F. Vakakis. Numerical and experimental investigations of a rotating nonlinear energy sink. *Meccanica*, 52(4-5):763–779, March 2016.

[12] Xilin Lu, Zhongpo Liu, and Zheng Lu. Optimization design and experimental verification of track nonlinear energy sink for vibration control under seismic excitation. *Structural Control and Health Monitoring*, 24(12), May 2017.

[13] Mohammad A. AL-Shudeifat and Adnan S. Saeed. Comparison of a modified vibro-impact nonlinear energy sink with other kinds of ness. *Meccanica*, 56(4):735–752, June 2020.

[14] Giuseppe Pennisi, Cyrille Stephan, Etienne Gourc, and Guilhem Michon. Experimental investigation and analytical description of a vibro-impact nes coupled to a single-degree-of-freedom linear oscillator harmonically forced. *Nonlinear Dynamics*, 88(3):1769–1784, January 2017.

[15] Tao Li, Sébastien Seguy, and Alain Berlioz. On the dynamics around targeted energy transfer for vibro-impact nonlinear energy sink. *Nonlinear Dynamics*, 87(3):1453–1466, October 2016.

[16] Tao Li, Claude-Henri Lamarque, Sébastien Seguy, and Alain Berlioz. Chaotic characteristic of a linear oscillator coupled with vibro-impact nonlinear energy sink. *Nonlinear Dynamics*, 91(4):2319–2330, December 2017.

[17] S. Lo Feudo, S. Job, M. Cavallo, A. Fraddosio, M.D. Piccioni, and A. Tafuni. Finite contact duration modeling of a vibro-impact nonlinear energy sink to protect a civil engineering frame structure against seismic events. *Engineering Structures*, 259:114137, May 2022.

[18] S. Luding. Granular materials under vibration: Simulations of rotating spheres. *Physical Review E*, 52(4):4442–4457, October 1995.

[19] Milton Abramowitz and Irene A. Stegun. *Handbook of Mathematical Functions with Formulas, Graphs, and Mathematical Tables*. Dover Publications, New York, 1965.

[20] Yunhyeok Han. *Innovative video-based techniques for outdoor vibration analysis of timber buildings*. PhD thesis, Université Paris-Saclay, 2024. Thèse de doctorat dirigée par Franck Renaud et encadrée par Stefania Lo Feudo et Gwendal Cumunel.

[21] Vieworks. *VC-101MX / VC-151MX User Manual*, 2019. Accessed on 2026-06-09.

A Test log

A.1 Configuration : OVINES2

Table 17: Common parameters for the experimental tests

Parameter	Value
Test date	29/04/2026
Camera acquisition frequency	800 fps
Trigger period	1250 μs
Camera opening window	100–900 μs
Camera resolution	4096×688 px
Camera offset	Offset X = 0 ; Offset Y (VW1 / VW2) = 1192 / 900
Accelerometers (sensitivity)	Channel 2: 10.4 mV/g ; channel 3: 10.35 mV/g

Table 18: Summary of the experimental test series

Test series	Shaker frequency	Shaker acceleration	Remarks
Test 1	11 Hz	$9g$	
Test 2	11 Hz	$9g$	
Test 3	11 Hz	$7g$	
Test 4	11 Hz	$7g$	
Test 5	11 Hz	$7g$	

A.2 Configuration : OVINES3

Table 19: Common parameters for the experimental tests

Parameter	Value
Test date	18/05/2026
Prototype used	Circular wall with a diameter of 100 mm
Camera acquisition frequency	800 fps
Trigger period	1250 μs
Camera opening window	100–900 μs
Camera resolution	4096×688 px
Camera offset	Offset X = 0 ; Offset Y = 1192
Accelerometers	Channel 2: 10.29 mV/g ; channel 3: 10.40 mV/g

Table 20: Summary of the experimental test series

Test series	**Shaker frequency**	**Shaker acceleration**	**Remarks**
Test 1	11 Hz	$8g$	No accelerometer data available.
Test 2	11 Hz	$8g$	
Test 3	11 Hz	$8g$	No accelerometer data available.
Test 4	11 Hz	$8g$	
Test 5	11 Hz	$8g$	
Test 6	11 Hz	$8g$	
Test 7	11 Hz	$7g$	
Test 8	11 Hz	$7g$	
Test 9	11 Hz	$6g$	
Test 10	11 Hz	$6g$	